

Simulated observations of star formation regions: infrared evolution of globally collapsing clouds

JESÚS M. JÁQUEZ-DOMÍNGUEZ ¹, ROBERTO GALVÁN-MADRID ¹, JACOPO FRITZ ¹, MANUEL ZAMORA-AVILÉS ²,
PETER CAMPS ³, GUSTAVO BRUZUAL ¹, MAARTEN BAES ³, YUXIN LIN ⁴ AND ENRIQUE VÁZQUEZ-SEMADENI ¹

¹*Instituto de Radioastronomía y Astrofísica, Universidad Nacional Autónoma de México, Morelia, Michoacán 58089, México.*

²*Instituto Nacional de Astrofísica, Óptica y Electrónica, Luis E. Erro 1, 72840 Tonantzintla, Puebla, México*

³*Sterrenkundig Observatorium, Universiteit Gent, Krijgslaan 281 S9, 9000 Gent, Belgium*

⁴*Max Planck Institute for extraterrestrial Physics, Gießenbachstraße 1, 85748 Garching, Bayern, Deutschland*

(Received; Revised; Accepted)

Submitted to ApJ

ABSTRACT

The direct comparison between hydrodynamical simulations and observations is needed to improve the physics included in the former and test biases in the latter. Post-processing radiative transfer and synthetic observations are now the standard way to do this. We report on the first application of the SKIRT radiative transfer code to simulations of a star-forming cloud. The synthetic observations are then analyzed following traditional observational workflows. We find that in the early stages of the simulation, stellar radiation is inefficient in heating dust to the temperatures observed in Galactic clouds, thus the addition of an interstellar radiation field is necessary. The spectral energy distribution of the cloud settles rather quickly after ~ 3 Myr of evolution from the onset of star formation, but its morphology continues to evolve for ~ 8 Myr due to the expansion of HII regions and the respective creation of cavities, filaments, and ridges. Modeling synthetic *Herschel* fluxes with 1- or 2-component modified black bodies underestimates total dust masses by a factor of ~ 2 . Spatially-resolved fitting recovers up to about 70% of the intrinsic value. This “missing mass” is located in a very cold dust component with temperatures below 10 K, which does not contribute appreciably to the far-infrared flux. This effect could bias real observations if such dust exists in large amounts. Finally, we tested observational calibrations of the SFR based on infrared fluxes and concluded that they are in agreement when compared to the intrinsic SFR of the simulation averaged over ~ 100 Myr.

Keywords: stars: formation — infrared: stars — infrared: ISM — methods: numerical — ISRF

1. INTRODUCTION

Star formation in the Universe is fueled by the gas in molecular clouds (MCs), but many questions remain unanswered. Only in recent years the advent of instrumentation that allows to perform multi-scale resolved studies has permitted to connect global to local scales (for a review, see [Motte et al. 2018](#)). An important topic of current research is to link our knowledge of star formation in the Milky Way and external galaxies (e.g., the review by [Kennicutt & Evans 2012](#)). MCs obscure optical starlight and emit themselves from near-infrared

(near-IR) to radio wavelengths. In the last two decades, infrared (IR) surveys of the Galactic plane using space telescopes such as *Spitzer* and *Herschel* have unveiled the star formation content of our Galaxy (e.g., [Churchwell et al. 2009](#); [Molinari et al. 2010](#)). Complementary ground-based surveys in the (sub)millimeter have been key to map the bulk of the mass in MCs as traced by their cold ($T \sim 10$ to 30 K) dust and molecular gas (e.g., [Schuller et al. 2009](#); [Aguirre et al. 2011](#)).

Important observational constraints now exist on the physics of star formation. Among the most important ones is that Galactic regions have been inferred to be inefficient in converting gas into stars, except possibly in their densest parts. The inferred – current – star formation efficiencies range from about zero to a few percent in nearby clouds (e.g., [Forbrich et al. 2009](#); [Evans](#)

et al. 2009) to $> 10\%$ for the most active clouds in the Milky Way (e.g., Galván-Madrid et al. 2013; Louvet et al. 2014; Ginsburg et al. 2016). Several theoretical scenarios for MC evolution and star formation have been able to reproduce a variety of observational restrictions (see, e.g., Federrath & Klessen 2012; Krumholz et al. 2012; Vázquez-Semadeni et al. 2019; Smith et al. 2020; Hennebelle et al. 2022). Among them, simulations of MCs that are under global collapse are particularly appealing for the regime of massive star formation in clustered environments (e.g., Vázquez-Semadeni et al. 2007; Heitsch & Hartmann 2008; Colín et al. 2013; Ibáñez-Mejía et al. 2016; Zamora-Avilés et al. 2019) since massive star-forming clumps appear to be dominated by self-gravity (e.g., Liu et al. 2012; Lin et al. 2016; Liu 2017). Ideally, such simulations should include the effect of ionizing feedback from young massive stars, which is one of the main ingredients responsible for stopping the otherwise runaway star formation and set the final star formation efficiency (e.g., Matzner 2002; Peters et al. 2010; Dale et al. 2012; Haid et al. 2019). Other factors that are important to determine the final star formation efficiency of a MC are initial conditions, such as cloud-scale magnetic fields and the amount of turbulence set by large-scale supernovae (e.g., Mac Low & Klessen 2004; Commerçon et al. 2011; Peters et al. 2011; Federrath & Klessen 2012), as well as other types of feedback such as stellar winds, bipolar outflows, and radiation pressure (e.g., Dale et al. 2014; Geen et al. 2021; Olivier et al. 2021; Rosen 2022).

However, theoretical models need further testing. An important limitation for a correct comparison between hydrodynamical simulations and observations is the barrier imposed by radiative transfer and instrument response. The post-processing calculation of the propagation of radiation across the MC and to the observer for the production of synthetic observations is becoming the standard technique to homogeneously compare simulations and observations (e.g., Arthur et al. 2011; Koepferl et al. 2017a; Betti et al. 2021; Izquierdo et al. 2021). A recent review on this topic is in Haworth et al. (2018). The comparison of synthetic observations of dust emission from the near to the far-IR is particularly useful because dust continuum emission is the most widely-used tracer of the interstellar medium (e.g., Koepferl et al. 2017b; Reissl et al. 2020; Liu et al. 2021). Such synthetic observations can be used to test how accurate are hydrodynamical simulations in recreating the physical properties of star formation regions. Conversely, synthetic observations can be used to test the observational techniques commonly used to calculate the properties of MCs. The comparison between the actual proper-

ties of the simulated clouds and the derived ones can be used to quantify the limitations and biases affecting these techniques.

In this work, we create and analyze radiative-transfer synthetic observations of the simulations presented by Zamora-Avilés et al. (2019). These models belong to what is known as the Global Hierarchical Collapse (GHC) scenario of MC formation and evolution (Vázquez-Semadeni et al. 2009; Vázquez-Semadeni et al. 2019). The simulation forms a young star cluster with massive star formation and ionization feedback. In Section 2 we describe the hydrodynamical simulation. In Section 3 we explain the methodology for the dust continuum radiative transfer. In Section 4 we outline the production of synthetic observations. In Section 5 we present our results, including a comparison to real observations. Finally, we discuss our results in Section 6 and give our conclusions in Section 7.

2. HYDRODYNAMICAL SIMULATION

The snapshots used in this work are taken from the radiation magnetohydrodynamical simulation presented in Zamora-Avilés et al. (2019), which follows the self-consistent formation and collapse of a cold molecular cloud from colliding flows in the warm neutral medium (WNM). We refer the reader to Zamora-Avilés et al. (2018) and Zamora-Avilés et al. (2019) for a complete description of the numerical methods in the hydrodynamical simulations. Here we briefly describe their setup.

The hydrodynamical simulation was performed in FLASH (V2.5; Fryxell et al. 2000). It includes magnetic fields, self-gravity, sink particles, and feedback by ionizing photons. The ionization feedback implemented in FLASH uses the “hybrid characteristics” approach adapted from Peters et al. (2010), which builds on the work by Rijkhorst et al. (2006). First, the hydrogen column density is calculated along rays from the sink particles, and the rate equation for the ionization fraction of the cells is solved along these rays. Heating and cooling are calculated separately for ionizing and non-ionizing radiation. We refer the reader to Zamora-Avilés et al. (2019) for a more detailed description of these implementations.

The size of the numerical box is of 256 pc in the x axis, and 128 pc in the y and z axes. The box initially contains warm neutral gas with uniform density and temperature of $n = 2 \text{ cm}^{-3}$ and $T = 1450 \text{ K}$. The initial composition is assumed to be purely atomic gas with molecular weight $\mu = 1.27$. Thus, the total mass within the box is $M_{\text{tot}} \approx 2.6 \times 10^5 M_{\odot}$. The grid refinement criterion employed is one of “constant mass”, in-

stead of the standard Jeans criterion. This means that, rather than maintaining a constant number of cells per Jeans length (which implies $\Delta x \propto \rho_{\text{thr}}^{1/2}$) we impose that the cell's mass is the same at each new refinement step (implying $\Delta x \propto \rho_{\text{thr}}^{1/3}$), and the maximum physical resolution reached is $\Delta x = 0.03$ pc.

The molecular cloud is formed by compression of two cylindrical flows from the WNM, as schematically depicted in Figure 1. The flows have radius $R_{\text{flow}} = 32$ pc and length $L_{\text{flow}} = 112$ pc, and move in opposite directions along the x axis with a supersonic velocity $v_{\text{flow}} = 7.5$ km s $^{-1}$. A background subsonic velocity field with a k^{-2} spectrum is imposed in the box with Mach number $\mathcal{M}_{\text{rms}} \approx 0.7$. Finally, the box is permeated by a magnetic field aligned along the x direction, with an initial uniform intensity of 3 μG , consistent with observations (Beck 2001).

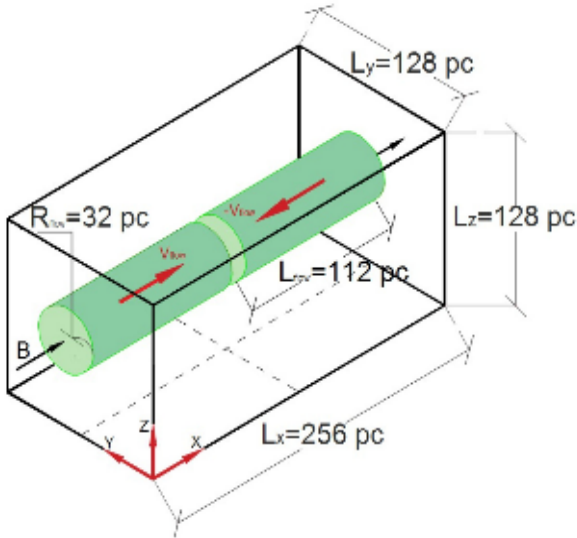


Figure 1: Sketch illustrating the initial conditions used in the simulations presented by Zamora-Avilés et al. (2019), which consist of two cylindrical streams colliding at the center of the numerical box.

Sink particles are formed in the simulation once a cell reaches the maximum level of refinement and the gas density within it is larger than a threshold value of $\rho = 8.9 \times 10^{-18}$ g cm $^{-3}$. The gaseous cell retains the excess mass above the density threshold, i.e., the initial sink particle mass is $M_{\text{sink}} = (\rho - \rho_{\text{thr}})\Delta x^3$. Then, the sink will continue to accrete mass from its surroundings within an accretion radius $\sim 2.5\Delta x$. Once the sink particles are massive enough, they start to inject ionizing photons into their surroundings, creating HII regions and sweeping out their surrounding gas.

The simulation snapshots analyzed in the radiative transfer post-processing presented here, are selected after the cloud undergoes a transition to the cold atomic phase, begins to contract gravitationally, and attains the temperature and density conditions typical of cold molecular clouds. The snapshots are selected to sample the following values of the cloud's instantaneous star formation efficiency (SFE), defined as the ratio of the mass in sinks over the total mass in sinks and gas. These correspond to values of the SFE from relatively quiescent clouds (e.g., Battersby et al. 2014; Wang et al. 2014; Lin et al. 2017) to active massive star formation regions (e.g., Lin et al. 2016; Motte et al. 2022; Traficante et al. 2023). The selected snapshots correspond to times $t = [0.8, 1.6, 3.3, 5.7, 6.3, 7.6]$ Myr after the first star is born, with the highest value approximately corresponding to the moment when feedback by supernovae might become relevant. This type of feedback is not included in the hydrodynamical simulation.

3. RADIATIVE TRANSFER

The post-processing radiative transfer (RT) was carried out with the Monte Carlo code SKIRT¹ version 9 (Camps & Baes 2015, 2020). This code includes the full treatment of absorption and multiple anisotropic scattering by dust and calculates the thermal emission self-consistently, also including the stochastic heating of the smallest dust grains. The code handles arbitrary three-dimensional (3D) geometry for both radiation sources and dust distributions, including grid-based representations generated by hydrodynamical simulations. In recent years, SKIRT has been used mostly to generate synthetic observations from hydrodynamically simulated galaxies (e.g., Camps et al. 2016; Elagali et al. 2018; Williams et al. 2019; Parsotan et al. 2021; Camps et al. 2022; Nanni et al. 2022). To our knowledge, this work is the first effort to expand the use of SKIRT to simulations of Galactic molecular clouds.

In SKIRT, a radiative transfer model is defined by the following components: *a)* the source system defined by the SED and spatial distribution of each of the primary sources of radiation; *b)* the dust system, in which the physical properties, composition, and spatial distribution of the dust are described; and finally, *c)* the synthetic instruments, which determine the wavelengths, position, and properties of the synthetic detectors. One of the improvements of SKIRT in version 9 is the possibility of having different wavelength grids for each component of the radiative transfer simulation. This allows

¹ <https://www.skirt.ugent.be>

to optimize the use of photon packages at the specific wavelengths where they are more important.

3.1. Source system

The hydrodynamical simulation does not resolve the formation of individual stars. Therefore, the sink particles have to be treated as stellar aggregates. To obtain the SED for the sources of stellar radiation we use the revised version of the [Bruzual & Charlot \(2003\)](#) stellar population synthesis models introduced in [Plat et al. \(2019\)](#), hereafter C&B models). The output SED of the stellar aggregate representing each sink particle depends on its total mass, age, metallicity, and the choice of a stellar initial mass function (IMF). The total mass, age, and position of each sink particle are known directly from the hydrodynamical simulation, while the metallicity is assumed to be solar. The C&B models make use of the PARSEC evolutionary tracks ([Bressan et al. 2012](#)). Finally, we adopt a [Kroupa \(2001\)](#) IMF with lower- and upper-mass limits of 0.1 and $100 M_{\odot}$, respectively.

An important point to keep in mind in the construction of the stellar aggregates is that the masses of the sink particles (up to a few $\times 10^2 M_{\odot}$) are not enough to fully sample the IMF. Thus, they cannot be considered simple stellar populations. For each sink particle, we need to distribute their total mass into individual stars using the IMF as a probability distribution function (see, e.g., [Bruzual 2010](#)). Due to the stochastic nature of populating the sinks in this way, any time that we create a realization of the stellar population for a sink, the SED will be different. To deal with these biases, for each sink particle we considered ~ 200 realizations of a stochastically-sampled IMF. We then produced the SED of each realization and calculated their bolometric luminosity. Finally, we used the spectrum with a luminosity closest to the median as the input SED for each sink particle at each snapshot.

Figure 2 shows the cumulative mass locked in sinks in the simulation as a function of time. Our radiative transfer simulations cover snapshots from a quiescent stage with little star formation up to an evolved massive stage with a total stellar mass of a few $\times 10^3 M_{\odot}$, which is comparable to the total mass in young stars in a molecular cloud such as Orion ([Da Rio et al. 2014](#); [Stutz 2018](#)).

Once we have characterized the SEDs of the sinks and their bolometric luminosities, we proceed to give them as input to SKIRT. The code distributes the total energy into photon packages with wavelengths between 0.01 to $2000 \mu\text{m}$ following a logarithmic spacing. These photons are then isotropically launched from the position of the sinks to the medium. The wavelength limits are chosen

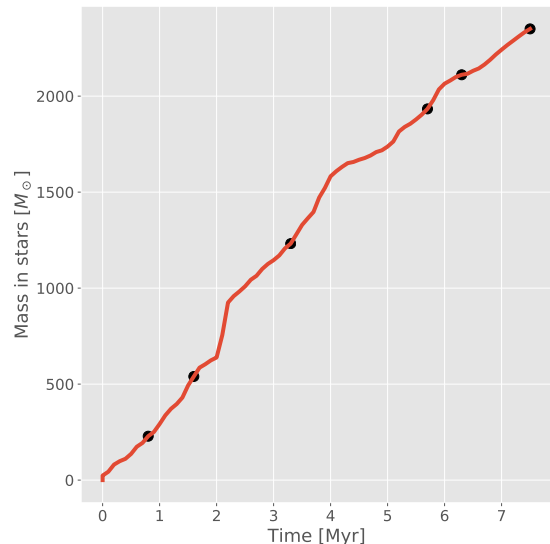


Figure 2: Evolution of the total mass in stars in the hydrodynamical simulation. The black dots show the age of the snapshots for which we have calculated the radiative transfer and created synthetic observations.

in such a way to include UV and optical photons that are the most important for dust heating, as well as IR emission from the primary sources of radiation.

Finally, we define the grid for the *radiation field*, which defines the wavelength points used to record the energy deposited by photon packets that interact with the dust in each cell. For this, we defined a grid with 50 bins distributed logarithmically in the ranges from 0.01 to $160 \mu\text{m}$. This allowed to optimize the use of computer memory, since the contribution to the dust heating due to photons with a wavelength greater than $160 \mu\text{m}$ is negligible. We refer the reader to section 5.4 of [Camps & Baes \(2020\)](#) for a more detailed description and justification of the wavelength grids.

3.2. Dust Model

SKIRT allows a flexible modelling of the dust composition. We chose the multi-component dust mix of [Draine & Li \(2007\)](#), which is appropriate for Milky Way dust. This dust mix is composed of silicates, – small – graphite, neutral and ionized polycyclic aromatic hydrocarbons (PAHs). The grain size range goes from $3.1 \times 10^{-4} \mu\text{m}$ to $2 \mu\text{m}$. The first two types follow a power-law size distribution, and the last one a log-normal. For each grain component, we use 15 size bins to discretize the calculations of the dust mix.

The gas cells from the hydrodynamical simulation are imported into SKIRT, which then converts the gas grid into a dust grid. We define the amount of dust in each cell M_{dust} as the amount of non-ionized gas multiplied

by the dust-to-gas ratio, which we take as 0.01 (Draine 2011):

$$M_{\text{dust}} = 0.01 M_{\text{gas}} (1 - F_{\text{ion}}), \quad (1)$$

where F_{ion} is the ionization fraction of the cell.

3.3. Synthetic instruments

The first instrument that we configured emulates an ideal spectrometer. The wavelength grid for this instrument is defined in a nested logarithmic way. The basic grid goes from 0.01 to 3000 μm and is divided into 250 bins. A high resolution sub-grid with 30 wavelength bins was also defined spanning the range from 1 to 35 μm , in order to better sample PAH emission and the 9.7 μm silicate absorption feature.

The second instrument that we used simulates a photometric camera that captures the surface brightness resulting from the Monte Carlo radiative transfer. We configured this camera with 4000×4000 pixels. The distance to the instruments was set to 5 kpc, which is an appropriate value for typical massive star formation regions in the Galaxy (Reid et al. 2014). This corresponds to an angular pixel size of $1.32''$ (0.032 pc), or about the maximum physical resolution of the hydrodynamical simulation. The total field of view of this camera is $88 \times 88 \text{ arcmin}^2$ (128 pc per side), which ensures the full coverage of the central part of the simulation (see Figure 1).

Although the radiative transfer models are designed to obtain results in a wide range of the spectrum (UV-radio), in this work we only analyze observations in the infrared, mainly to simulate photometric instruments of the *Spitzer* and *Herschel* observatories.

3.4. ISRF model

The earlier snapshots in which most of the stars are not yet born, or are still deeply embedded, should have in principle properties similar to those of the infrared dark clouds (IRDCs) observed in the Galaxy (Rathborne et al. 2006). These IRDCs have gas and dust temperatures as low as ≈ 10 K (Pillai et al. 2011; Battersby et al. 2014; Wang et al. 2014; Lin et al. 2017). However, the hydrodynamical simulation does not include the sources that produce early dust heating in the molecular cloud. To achieve realistic initial temperatures, we include an additional source of photons simulating a kind of interstellar radiation field (ISRF). This ISRF is included in the form of a shell of 64 pc radius that radiates inward only. The SED of the ISRF is constructed using the parametrization of Hocuk et al. (2017). This consists of the sum of six modified black bodies (Zucconi et al. 2001) plus an UV contribution (Draine 1978). Each of

Table 1: Parameters for the six modified black bodies from the non-UV ISRF.

$\lambda[\mu\text{m}]$	W_i	T_i K
0.4	1×10^{-14}	7500
0.75	1×10^{-13}	4000
1	4×10^{-13}	3000
10	3.4×10^{-9}	250
140	2×10^{-4}	23.3
1060	1	2.728

the blackbody parts can be characterized as:

$$J_{\nu}^{\text{no-UV}} = \frac{2h\nu^3}{c^2} \sum_i \frac{W_i}{\exp(h\nu/K_B T_i) - 1}, \quad (2)$$

where the values for W_i and T_i are given in Table 1. The UV part of the spectrum is adopted from Draine (1978), rewritten in the following form to match units:

$$J_{\nu}^{\text{UV}} = 4280(h\nu)^2 - 3.47 \times 10^{14}(h\nu)^3 + 6.96 \times 10^{24}(h\nu)^4. \quad (3)$$

The combined radiation field is given by:

$$J_{\nu}^{\text{ISRF}} = J_{\nu}^{\text{no-UV}} + J_{\nu}^{\text{UV}}. \quad (4)$$

In Eqs. 2, 3, and 4 the mean intensities are in $\text{erg s}^{-1} \text{ cm}^{-2} \text{ Hz}^{-1} \text{ sr}^{-1}$, and all other quantities are also in cgs units.

The impact of not including the ISRF as an extra source of radiation is more evident in snapshots previous to the formation of massive sinks. In these early time steps, HII regions have not started to sweep their surrounding dense gas, and the UV-optical photons cannot escape to distances beyond a fraction of a pc. Without the ISRF which permeates the cloud from the outside, in these early snapshots the stellar radiation field is reprocessed only by dust in the immediate surroundings of the – fewer – young stars. Therefore, the photons that exit from these compact dust cores are predominantly at IR wavelengths, thus are inefficient to heat the dust across the entire cloud. The result of this is that the bulk of the cloud mass is kept at temperatures of a few Kelvin, which is unrealistically low.

As we described in Section 3.1, the sources in SKIRT are defined by the shape of the SED and its normalization, which in this work we are using the bolometric luminosity. The form of the ISRF has already been defined using the Equation 4. Then, taking advantage of the fact that we can define the bolometric luminosity by hand, we perform different simulations where we vary the value of the ISRF luminosity in order to simulate that our cloud is surrounded by different environments and thus

Table 2: Luminosity input of the primary radiation sources in the radiative transfer models and the resulting mass-weighted dust temperature for the cloud in the earliest snapshot at 0.8 Myr.

Model	Luminosity	Dust temperature
0.8 Myr	$[L_{\odot}]$	[K]
STARS	1.47×10^4	3.73
ISRF	10^4	6.21
ISRF+ STARS	2.47×10^4	8.69

see how the temperature of our cloud changes. We generate three different models for the earlier 0.8 Myr snapshot. To quantify the difference between models we use the mass-weighted average temperature, which is calculated by multiplying the mass and the temperature over the grid. The first model, which we call STARS, uses only the sinks as photon sources. The total sink luminosity input for this model is $L_{\text{stars}} = 1.47 \times 10^4 L_{\odot}$. The resulting mass-weighted average temperature across the cloud is only 3.73 K. For the next model, ISRF, we only use the ISRF as a source of radiation. The ISRF luminosity is $L_{\text{ISRF}} = 10^4 L_{\odot}$. The resulting mass-weighted temperature is 6.21 K. Finally, the model where we include both sources of radiation, ISRF+STARS, has resulting mass-weighted temperature is 8.69 K, which is more consistent with the ~ 10 K expected from observations.

The previous test illustrates our point that the ISRF is needed, and indeed it dominates dust heating across the cloud during earlier stages of the simulation prior to significant stellar feedback. In Table 2 we summarize the results of these tests. For the model where we include the ISRF and stars, we test decreasing the total ISRF luminosity to $\sim 10^3 L_{\odot}$ and found that the mass-weighted average cloud temperature is reduced to 4.55 K, while if we increase to values much larger than $10^4 L_{\odot}$ does not result in a significant increase in dust temperature. Therefore, we fix $L_{\text{ISRF}} = 10^4 L_{\odot}$.

4. SYNTHETIC OBSERVATIONS

4.1. Synthetic SED

In this section, we describe the raw SEDs resulting from the radiative transfer simulations. For this, we analyze the output SED from the instrument that simulates an ideal spectrometer, which captures the photons that leave the region in the whole spectral range. This instrument has an infinite aperture and is configured with the wavelength grid defined in Section 3.3. Figure 3 shows the resulting ideal SED for the face-on and

edge-on views² of the cloud for the different timesteps, as well as the input-source SEDs.

The first interesting feature that stands out in both lines of sight, is seen in the SED of the 0.8 Myr snapshot (red line), which shows very low UV-optical emission (at 0.1 to 1 μm). Instead of the typical stellar emission (dotted line), we see a “blackbody shape” that peaks between 1 to 2 μm in near-IR H band. Comparing the cloud SED with the input ISRF we can see that almost all of the cloud emission at shorter wavelengths is due to the latter. Emission that is reprocessed by the dust in the cloud, both from the ISRF and the few young stars, shines as a second peak in the cloud SED at $\sim 70 \mu\text{m}$ (see Fig. 3). The cloud emission toward longer wavelengths (100 to 1000 μm) comes from dust far from the input sources that remains at lower temperatures, as well as from photons from this part of the ISRF spectrum that do not interact with the ISM. Strictly speaking, the latter contribution to the observed SED is not cloud emission. In our observational treatment of the synthetic images we eliminate this artefact by means of background subtraction (see Section 4.2). Finally, characteristic emission from PAHs is visible at around 6.2 μm , as well as the silicate feature at 9.7 μm .

In the second time step (1.6 Myr) we see that stellar emission at $< 1 \mu\text{m}$ starts to contribute to the SED. This is more evident in the face-on view, for which the dust surface density in the line of sight is smaller with respect to edge-on. In both lines of sight, PAH emission and silicate bands at ~ 3.6 , 6.2, and 9.7 μm are all now well-defined. An interesting feature of this SED is the shape in the mid- to far-IR wavelengths range (~ 20 to 500 μm), where emission is nearly flat in the log-log representation. This indicates that the dust in the cloud has a wide range of temperatures from ~ 10 to 100 K similarly contributing to the observed flux.

For the remaining snapshots at 3.3, 5.7, 6.3, and 7.5 Myr, the stellar emission becomes more significant as a consequence of stellar-mass growth (see Fig. 2). The effect of HII region feedback, which sweeps up material exposing the stellar sources, is also a contributing factor. As the cloud evolves, more sinks are formed and the protostellar cores are dispersed, allowing more stellar UV and optical photons to reach the instrument. The PAH features remain prominent and the global peak of the SED remains in the far-IR around at $\sim 160 \mu\text{m}$, dominated by dust at ~ 20 K. Overall, the cloud SED converges to an almost constant shape after ~ 3 Myr of evo-

² The face-on and edge-on views are defined along the x and y axes of Figure 1, respectively.

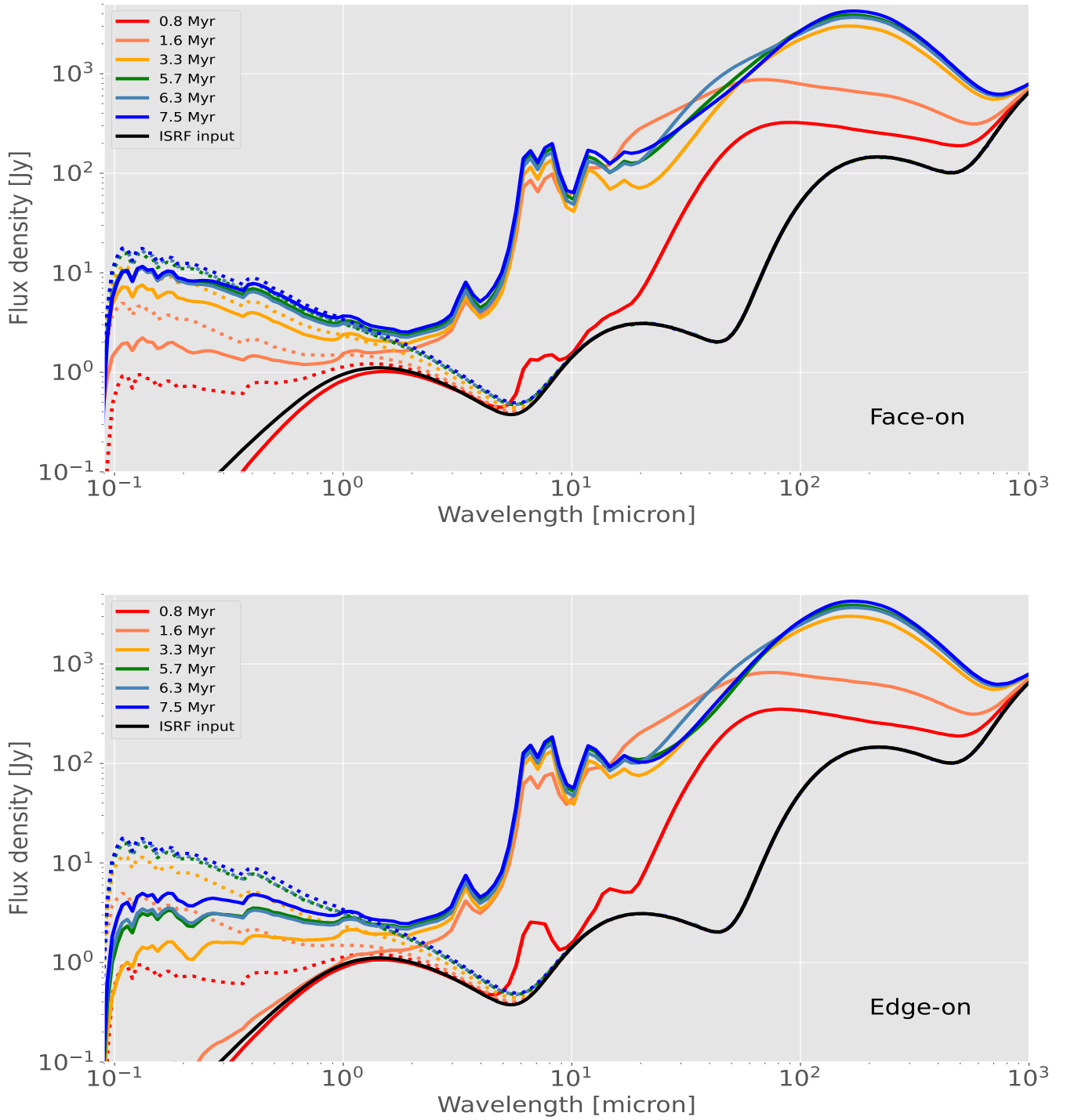


Figure 3: SEDs resulting from the ideal synthetic observations. The upper panel shows the SED observed for the face-on line of sight. The lower panel shows the edge-on view. The colored full lines show the resulting cloud SED for the different snapshots. The dotted lines represent the respective total SED (stars + ISRF) of the input sources. The solid black line highlights the input SED of the ISRF source alone.

lution from the onset of star formation, as marked by the first appearance of sink particles. This timescale is appropriately bounded in the lower end by the ~ 1 Myr of the added lifetimes of massive young stellar objects and ultracompact HII regions (Motte et al. 2018; Kalcheva et al. 2018), and in the higher end by estimates of a few Myr for the coexistence of massive stars and molecular clouds before dispersal (Vázquez-Semadeni et al. 2018; Chevance et al. 2020).

4.2. Synthetic broadband images

SKIRT produces idealized synthetic images in selected broadband filters. We simulated observations in the IR, so the broadband used for this work comes principally from *Spitzer* and *Herschel* observatories, and are listed in Table 3. The left panel of Figure 4 shows an example of an idealized output image for the PACS 70 μm band from the 3.3 Myr snapshot. To include the effects of the spatial instrument response we convolve the SKIRT output images with an approximate point spread function (PSF). We choose 2D Gaussian kernels with full width at half-maximum (FWHM) matched to the PSF of each combination of instrument and band (see Table 3). We call the resulting image an *intermediate synthetic observation*, exemplified in the central panel of Figure 4 for the PACS 70 μm band.

We subtract a contribution from the foreground and background emission – hereafter just called “background” for simplicity – from the intermediate synthetic observations. This background is the sum of dust emission outside of 100 pc central cube plus artificial background emission due to the geometry of our implementation of the ISRF. The latter artificial background comes from the ISRF photons that reach the synthetic camera without interacting with any dust in the grid (see Section 3.4). To define the background in each of the intermediate synthetic observations, we choose a central sub-region of 68.75×68.75 arcmin² from the total 88×88 arcmin² image. This sub-region is called the *observed cloud* and is represented as a yellow box in the central panel of Figure 4. The background is then defined as the average intensity outside the observed cloud and is subtracted from the flux of the intermediate synthetic observation. We call this background-subtracted sub-image the *synthetic observation*, as shown in the right panel of Figure 4. These are used to extract photometry and derive the physical properties of the simulated clouds in such a way to mimic observational methods.

5. ANALYSIS

The advantage of dealing with numerical simulations is that their physical properties are explicitly known.

Table 3: Photometric bands used to create the synthetic observations from the radiative transfer simulations. Taken from De Looze et al. (2014).

Band	λ [μm]	FWHM [arcsec]
IRAC 3.6	3.6	1.7
IRAC 4.5	3.6	1.7
IRAC 5.8	5.8	1.9
IRAC 8.0	8.0	2.0
WISE 3	12	6.5
MIPS 24	24	6
PACS 70	70	5.8
PACS 100	100	6.8
PACS 160	160	12.1
SPIRE 250	250	18.2
SPIRE 350	350	24.9
SPIRE 500	500	36.3

Therefore, we can apply standard analysis techniques to the synthetic observations and check their ability in recovering properties such as the dust mass and temperature. In this section we perform an analysis of the synthetic observations: we measure the far-IR fluxes and fit them with a modified blackbody model, then derive the corresponding dust mass and temperature. We perform the analysis both for the full cloud fluxes and in a spatially-resolved manner.

5.1. Observed synthetic SEDs and comparisons to observations

For each snapshot of the hydrodynamical simulation, we have produced *synthetic observations* in the 12 IR bands listed in Table 3. We extract the fluxes from these using the previously defined instrumental aperture of 100 pc per side (see Section 4.2). Hence, for each time step, we can construct the respective *observed synthetic SED*. Figure 5 shows these from mid- to far-IR for the edge-on and face-on line of sights.

Figure 5 also shows the observed SEDs of a sample of active massive star forming clouds taken from Binder & Povich (2018), as well as a sample of infrared dark clouds (IRDCs) presented by Lin et al. (2017). All the SEDs were scaled to the average distance (2.9 kpc) of the Galactic sample to enable a more direct comparison. The observed synthetic SEDs follow the same time evolution described for the raw SEDs in Section 5.1, but with coarser detail. Once the ISRF is removed via background subtraction, we can assume that the emission at

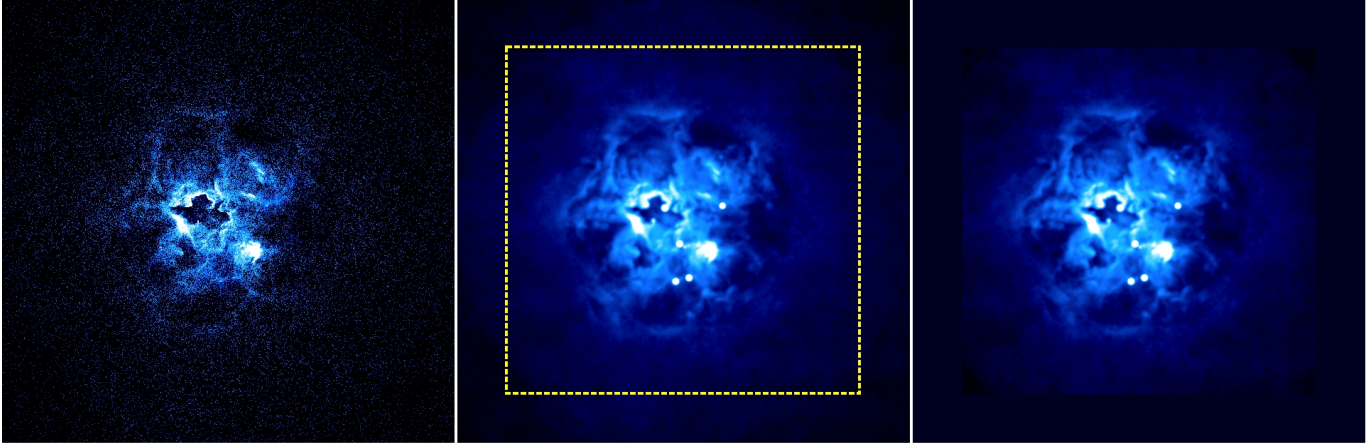


Figure 4: Sketch of the process to obtain a background-subtracted *synthetic observation*. The *left* panel shows a raw SKIRT output image. The *middle* panel shows an *intermediate synthetic observation* after convolution with the PACS 70 μm PSF. A yellow box separates the *observed cloud* from the outer region where the *background* is defined. The *right* panel shows the *synthetic observation* after background subtraction. The color scale is arbitrary to highlight the molecular cloud features. This snapshot corresponds to 3.3 Myr after the first star is born.

these wavelengths is purely from the star formation region.

In the first time step at 0.8 Myr, when the stellar radiation from the relatively low mass stellar population is still deeply embedded, the peak of the SED is at $\sim 70 \mu\text{m}$, and the emission is dominated by warm dust (at $\geq 40 \text{ K}$) that is very close to the newly formed stars. In the second time step, at 1.6 Myr, the cloud luminosity at $24 \mu\text{m}$ becomes relevant, even slightly larger than at later times in this band. This represents the transition from dense cores of molecular gas to small HII regions. Hence, in this phase we observe significant mid-IR emission caused by dust around the young HII regions that start to expand (e.g., Deharveng et al. 2010; Anderson et al. 2014). The peak of emission is still around $\sim 70 \mu\text{m}$.

One would expect the synthetic observations of the two earlier snapshots to resemble the SEDs of young objects such as IRDCs, where the emission is dominated by cold dust peaking around $\sim 250 \mu\text{m}$ (e.g., Pillai et al. 2011; Battersby et al. 2014; Lin et al. 2017). Instead, the shape of those SEDs does not resemble any observed Galactic region. We believe this to be an artifact of the models, since the young ($\leq 1 \text{ Myr}$) sinks are populated with main sequence stars rather than protostars, which will have a colder photospheric spectrum (Hosokawa & Omukai 2009).

Once the material around the massive stars is swept away by the ionizing feedback, UV-optical photons can travel further and heat the dust in the entire simulation grid. This is why the peak of the emission for these

synthetic SEDs is around $\sim 160 \mu\text{m}$, consistent with the Galactic sample. Also, the sinks in these snapshots are old enough to ensure that they are correctly populated with stars already in the main sequence.

5.2. Modified blackbody fits to the SEDs

Modified black body (MBB) fitting using far-IR images is widely used to derive integrated dust properties such as mass, temperature, and emissivity index. We now apply these classical methods to the synthetic photometry of the simulated cloud. To do so, the far IR *Herschel* bands were fitted using MBB (either 1 or 2 components) under the assumption of optically thin dust emission. The general form of a MBB is given by:

$$S_\nu = \frac{M_{\text{dust}}}{d^2} \kappa_\nu B_\nu(T_{\text{dust}}), \quad (5)$$

where M_{dust} is the dust mass, κ_ν is the dust opacity, d is the distance to the cloud, and $B_\nu(T_{\text{dust}})$ is the Planck function at a dust temperature T_{dust} .

The frequency-dependent dust opacity was assumed to follow a power-law of the form:

$$\kappa_\nu = \kappa_0 \times \left(\frac{\nu}{\nu_0} \right)^\beta, \quad (6)$$

where β is the dust emissivity index.

We use the same dust optical properties as in the radiative transfer simulations (Draine & Li 2007). From a fit to the far-IR opacities, we obtain an emissivity index $\beta = 2.08$ and an opacity at $350 \mu\text{m}$ $\kappa_0 = \kappa_{350} = 2.58 \text{ cm}^2 \text{ g}^{-1}$, which will be kept constant in the rest of

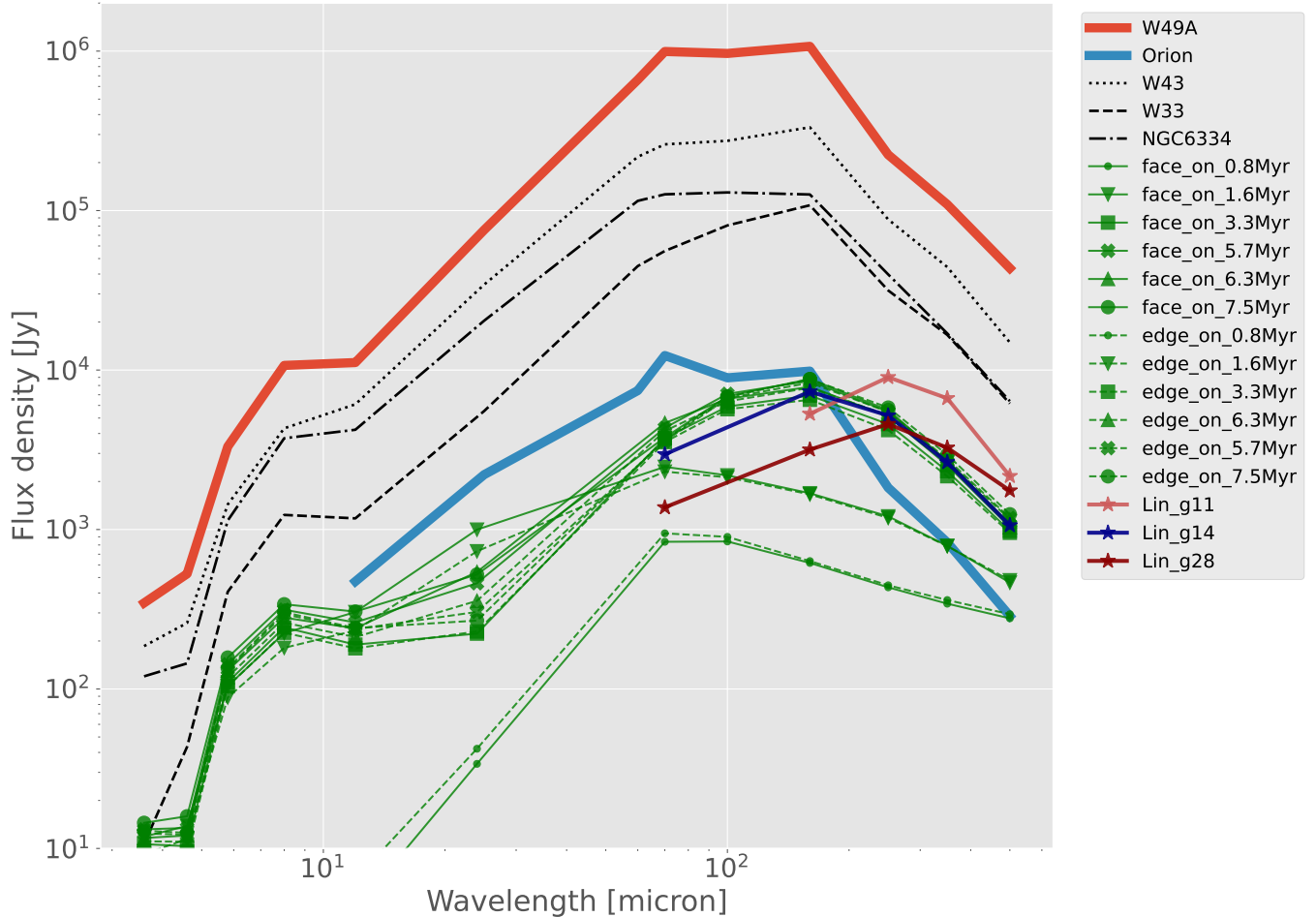


Figure 5: Comparison between the observed synthetic SEDs and those of Galactic star formation regions. Green lines show the synthetic SEDs for the face-on (solid lines) and edge-on (dashed) model views. Timesteps in the models use different markers. The lines without markers are SEDs from active clouds in the sample of [Binder & Povich \(2018\)](#), while the colored lines with star markers are SEDs from the IRDC sample of [Lin et al. \(2017\)](#). All the fluxes have been scaled to a distance of 2.9 kpc.

this work. Therefore, the only free parameters in the MBB fit will be the dust mass and temperature. The fit was performed with the python module `lmfit` ([Newville et al. 2021](#)).

As we have mentioned in Section 4, the SEDs of the first two timesteps at 0.8 and 1.6 Myr do not have the characteristic modified blackbody shape and are in fact rather flat. For this reason, no acceptable MBB fits could be obtained for these two snapshots. For the rest of the timesteps, the SED shape is very close to the typical MBB emission, therefore the simulated data are well represented by this model. First, we performed the fit using a single temperature MBB to calculate the properties of the cloud using the 160 to 500 μm bands. This approach is frequently used where the observations at 70 and 100 microns are not available (e.g., [Alves de Oliveira et al. 2014](#); [Ladjelate, B. et al. 2020](#); [Potdar et al. 2022](#)). The resulting mass and temperature with this model are shown in the right part of Table 4.

We also used the slightly more general approach of including data points at 70 and 100 μm and performing the photometry fitting. This allows to recover dust mass in a second (warmer) component at ~ 30 K, in addition to the colder component at ~ 15 K. The resulting total dust masses following this resolved 2-temperature MBB approach are listed in the left part of the Table 4, for both lines of sight. The dust masses derived in this way are systematically larger compared to those obtained using a single MBB. This is due to the fact that, in the 2-temperature model, the temperature of the colder component is lower than the dust temperature of the single-component MBB. Therefore, a larger cold-dust mass is needed to reach the observed flux levels.

In both types of fitting, the derived masses for the last 3 snapshots are larger for the edge-on view than for face-on. This is because in the face-on view the warmer dust in the immediate vicinity of the radiating stars is

Table 4: Masses and temperatures calculated from the modified blackbody fits for the two lines of sight. The second column shows the mass in the 100 pc cubic central box calculated directly from the dust simulation dust grid.

Intrinsic		Two modified BB						Single modified BB			
		face-on			edge-on			face-on		edge-on	
Snapshot	$M_{100\text{pc}}$	mass	T_{warm}	T_{cold}	mass	T_{warm}	T_{cold}	mass	T	mass	T
Myr	$10^2 M_{\odot}$	M_{\odot}	K	K	M_{\odot}	K	K	M_{\odot}	K	M_{\odot}	K
0.8 ^a	8.89	—	—	—	—	—	—	—	—	—	—
1.6 ^a	8.93	—	—	—	—	—	—	—	—	—	—
3.3	8.92	527 ± 74	29.8 ± 2.3	15.1 ± 0.9	531 ± 80	28.8 ± 1.8	14.6 ± 0.9	422 ± 20	17.1 ± 0.2	409 ± 30	16.9 ± 0.3
5.7	9.01	512 ± 68	30.8 ± 3.3	16.1 ± 1.0	635 ± 93	27.3 ± 1.9	14.9 ± 1.0	433 ± 16	17.7 ± 0.2	508 ± 29	17.0 ± 0.3
6.3	9.00	506 ± 66	33.6 ± 3.6	16.0 ± 0.9	626 ± 85	30.5 ± 2.4	15.1 ± 0.8	430 ± 15	17.4 ± 0.2	514 ± 30	16.7 ± 0.3
7.5	9.10	500 ± 65	30.1 ± 3.8	16.4 ± 1.1	655 ± 92	28.0 ± 2.3	15.2 ± 1.0	432 ± 14	17.8 ± 0.2	541 ± 28	17.0 ± 0.2

^a Values are not reported because the fit is not reliable.

directly seen. Indeed, for these snapshots we observe that fluxes for the face-on view are larger at wavelengths $< 160 \mu\text{m}$, as compared to those for the edge-on view. Therefore, the global temperature obtained by the MBB fit is slightly larger in the face-on view (see Table 4), and a slightly lower mass is needed to fit the synthetic photometry.

5.3. Comparison to intrinsic dust masses

In the previous section we have applied standard analysis techniques such a modified black body fitting, to check their ability in recovering dust properties such as mass and temperature. We have found that this method systematically underestimates the “real” mass by at least 30% in the best case scenario (see Table 4).

With the aim of analyzing where the differences come from, we have calculated the cumulative mass as a function of temperature from the cells inside the SKIRT dust grid to see what is the amount of dust mass that is too cold to provide a significant contribution in the far-IR *Herschel* bands. To be consistent with the definition of *observed cloud* from Section 4.2, we use the radiative transfer simulation grid to calculate the mass of dust inside a cube of 100 pc length, that we will dub as $M_{100\text{pc}}$. In the second column of Table 4 we show $M_{100\text{pc}}$ for the different snapshots.

Figure 6 shows the cumulative mass function for cells with temperature below a given threshold, for the case of the 3.3 Myr snapshot. The total dust mass recovered from the 2-MBB fits is also shown. The intersection occurs at about 13 K, showing that dust with temperature lower than this value will have an increasingly smaller contribution to the observed far-IR flux.

To be able to estimate the contribution to the far-IR flux of the coldest cells, we create a toy model where each cell inside the $M_{100\text{pc}}$ cube emits as a modified blackbody with mass and temperature given by the properties of the cell. We define as “cold” cells those with

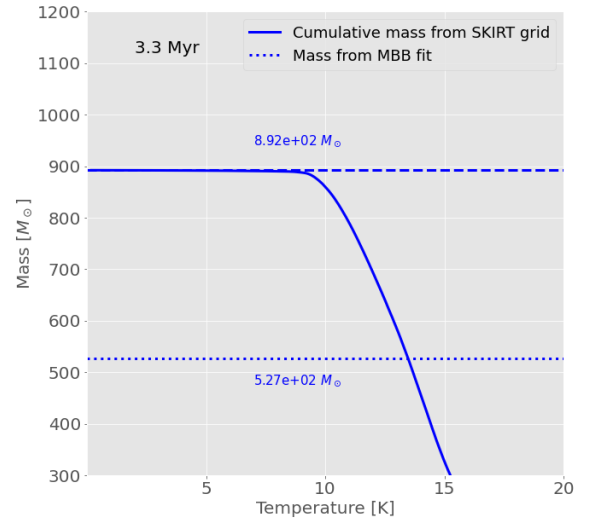


Figure 6: Cumulative dust mass in the SKIRT grid for the 3.3 Myr snapshot, within a box of $M_{100\text{pc}}$ (solid line). The total mass within this grid (horizontal dashed line) and the total recovered mass from the 2-MBB fits (horizontal dotted line) are also shown for comparison. The intersection between fitted and intrinsic mass occurs at 13.5 K.

$T \leq 15 \text{ K}$, and as “warm” those with $T > 15 \text{ K}$. Then, for each of the two components, we calculate both their dust mass and far-IR fluxes from 70 to $500 \mu\text{m}$. In Table 5 we show the results of this experiment as contribution percentages of mass and bolometric far-IR flux for both the cold and warm components. We can see that the bolometric flux is dominated by the warm component, which contributes with $\sim 90\%$ of the total emission at each snapshot. The cold component, whose mass is around $37 - 63\%$ of the total, only contributes with $\sim 10\%$ of the flux.

Table 5: Percentage of contribution to the total mass and far-IR flux for the “cold” ($T \leq 15$ K) and “warm” ($T > 15$ K) dust cells.

Time	Cold	Cold	Warm	Warm
Myr	mass	flux	mass	flux
	%	%	%	%
0.8	99.57	7.44	0.43	92.56
1.6	96.20	13.40	3.80	86.30
3.3	63.33	11.90	36.67	88.10
5.7	47.03	9.32	52.97	90.68
6.3	47.68	10.21	52.32	89.79
7.5	37.72	8.21	62.28	91.79

In Figure 7 we show the SEDs of these two components, obtained as the sum of the MBB models for each cell. In the youngest snapshot, the emission of the warm component dominates the IR SED at all wavelengths $< 250 \mu\text{m}$, where the cold dust emission kicks in. Interestingly enough, at the later time steps, it is the warm dust that dominates the emission up to at the longest wavelengths. It is also worth noting that the difference in wavelength of the two emission peaks decreases monotonically with time, probably due to a more homogeneous dust temperature distribution. The comparable luminosities of the two components at 0.8 and 1.6 Myr also explains why the SEDs are very flat in these snapshots.

In summary, the presence of very cold cells that are underluminous in the far-IR explains the difference between the “real” mass in the hydrodynamical simulation and the one derived from MBB fits. We consider this to be a real effect that could bias observations.

5.4. Pixel by pixel fit

An advantage of dealing with spatially resolved data is that it is possible to perform pixel-by-pixel MBB fitting. One can then obtain maps of the dust surface density and temperature for the region under scrutiny. In unresolved observations the properties that we recover are inevitably luminosity-weighted ones, therefore a clear advantage of resolved analysis is that we are able to follow the morphological evolution of these quantities by analyzing changes in the synthetic maps of the different timesteps of the hydrodynamical simulation.

In order to perform this analysis, we convolve all the *synthetic observations* to the $500 \mu\text{m}$ *Herschel* PSF, to match them in angular resolution. To optimize the calculations, we regrid the images in such a way that one pixel roughly corresponds to $1/3$ of the PSF width. Like this, we go from a pixel scale of $1.32''$ to $12.1''$. Since in the construction of the synthetic observations we per-

formed a background subtraction, it is possible that some pixels will end up having very low or even negative fluxes. Hence, we only consider pixels with flux density > 1 mJy to ensure all bands can be used. Furthermore, when analyzing the results, we discard those pixels with $\chi^2 \geq 10$, for which dust properties are likely not well constrained.

We use a single temperature MBB to reproduce emission within the $160 - 500 \mu\text{m}$ range. The resulting maps of dust surface density and temperature for the face-on line of sight are shown in Figures 8 and 9, respectively.

Next, we analyze the surface density maps for the different snapshots. In the first time step (upper-left panel of Figure 8) the vast majority of pixels have a poor fit. As mentioned before, the reason is that at wavelengths $\lambda \gtrsim 200 \mu\text{m}$ their SED is basically flat. Therefore, the surface density maps could not be determined for the most part. Figure 13 in Appendix A shows an example SED of a pixel with a bad fit due to the above-mentioned issue.

As the cloud evolves to 1.6 and 3.3 Myr (top center and right panels in Figure 8), we see that more sinks start to appear around the central massive one. Even though the newly formed sinks are of low mass ($< 50 M_{\odot}$), the additional luminosity that they inject is enough to heat dust over more extended areas, and at 3.3 Myr this heated dust already appears in the recovered maps over almost the entire cloud. We note that in this snapshot the surface density around the most massive sink in the center has already started to decrease, as a consequence of the first appearance of its corresponding HII region.

Since the dust density in our radiative transfer models is proportional to the complement of ionized gas in each cell, the dust disappears once the gas has been completely ionized by the massive stars, and thus the model HII regions have no IR emission. This is why dust surface density cavities become evident in the lower panels of Figure 8. Another consequence of the formation of the HII regions is that they push neutral material and create overdensities in their periphery. An example of this is the overdensity or ridge that becomes prominent in the bottom-left panel of Figure 8, created by the HII regions labeled R1 and R4 by Zamora-Avilés et al. (2019). Over the last two snapshots, at 6.3 and 7.5 Myr, the HII regions continue their expansion, and it is seen how the sinks that are born within the triggered ridge start to disrupt their parental cloud.

During the last three snapshots shown in Figure 8, the triggered ridge becomes smaller but does not totally disappear. Several effects are in place here. The first is evolutionary. Most of the sinks that are located

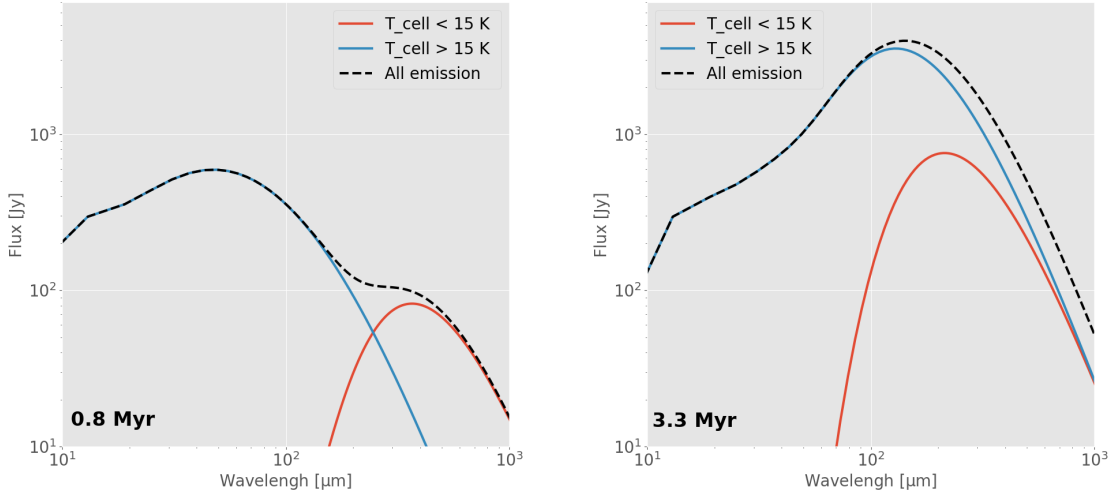


Figure 7: Resulting SEDs for the toy model described in Section 5.3. The blue and red lines show the SEDs of the “warm” and “cold” components, respectively. The black dashed line is the sum of the two components. The left panel shows the earliest snapshot at 0.8 Myr. The right panel corresponds to a more evolved snapshot at 3.3 Myr.

close to this ridge are born at later stages of the simulation, and further gas dispersal is yet to happen. In fact, the same happens to the central region (R1), which contains massive sinks already in the 3.3 Myr snapshot, but develops a prominent cavity until later. Second, the formation of this ridge appears to be due to triggering (e.g., Deharveng et al. 2012) by the collective action of the surrounding sinks. Third, feedback from some of these sinks appears to act more efficiently toward the outward direction of the cloud, where secondary cavities appear. And finally, a projection effect. We note how these (column density) cavities are evident in the face-on views (Fig. 8) but not when the cloud is viewed edge-on (Fig. 14).

This description from synthetic observations is consistent with the analysis of Zamora-Avilés et al. (2019). Note that the morphological evolution described above is much harder to detect and follow if the cloud is viewed edge-on (see Figure 14 in Appendix B).

We also calculated the total dust masses from the spatially resolved maps using pixel-by-pixel 2-temperature MBB fitting. A comparison of the results is shown in Table 6. The use of 2 MBB components allows to recover $\sim 10\%$ more mass than with only 1 MBB, likely because in some single resolved regions the smaller flux contribution of the coldest cells (see Section 5.3) can be recovered.

We now describe the dust temperature evolution. Figure 9 shows the inside-out evolution of dust heating by star formation as the cloud evolves in time. In the snapshot at 3.3 Myr, the stellar radiation field is already

snapshot	$M_{100\text{pc}}$	1 MBB	2 MBB
Myr	$10^2 M_{\odot}$	M_{\odot}	M_{\odot}
0.8	8.89	—	—
1.6	8.93	142.81	602.74
3.3	8.92	486.07	584.31
5.7	9.01	498.49	585.61
6.3	9.00	496.21	576.17
7.5	9.10	518.21	599.53

Table 6: Total masses calculated using pixel-by-pixel MBB fitting for both the single and 2-temperature MBB models in the face-on line of sight.

strong enough to heat the entire cloud. At this time, 76 % of the pixels show temperatures between 12 and 18 K, the average temperature being around 14.8 K. The pixels with the highest temperature (~ 30.5 K) are located around the massive star formation sites, and we can see a gradient in temperature from the stars to the edge of the cloud.

In the following snapshots at 5.7, 6.3 and 7.5 Myr (bottom panels of Figure 15), 79 % of the pixels with valid fits have temperatures between 12 and 18 K, the mean temperature is now ~ 15.5 K and the maximum temperature is ~ 33.3 K.

5.5. Star formation rate

One of the most important physical properties of molecular clouds is the rate at which they form stars. Mathematically, the SFR is defined as the mass of stars

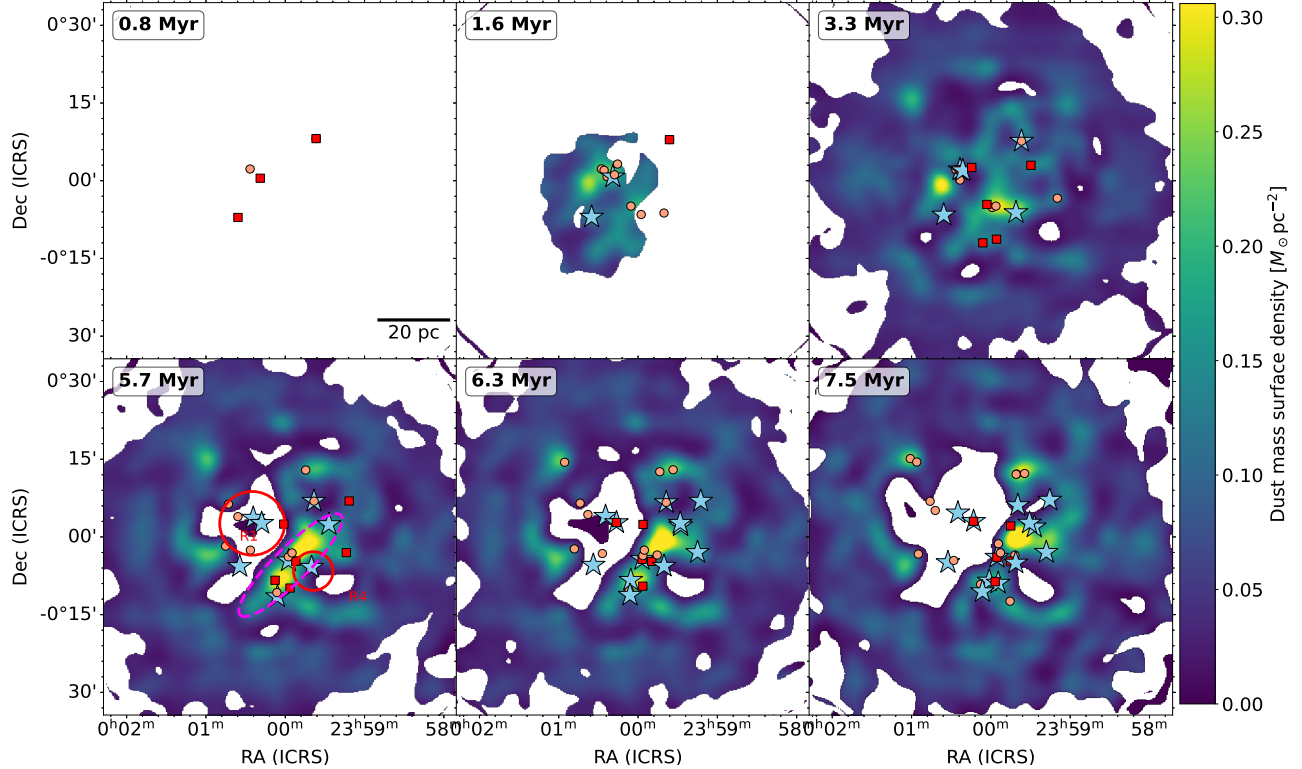


Figure 8: Dust surface density maps ($M_{\odot} \text{pc}^{-2}$) resulting from the spatially resolved fitting to the face-on synthetic observations at various timesteps. The markers represent the projected sink positions, where blue stars are used for sinks with masses $\geq 100 M_{\odot}$, red squares for sinks with masses between $50 M_{\odot}$ and $100 M_{\odot}$, and orange circles the sinks with $\leq 50 M_{\odot}$. In the bottom left panel, the magenta dashed ellipse represents the overdensity formed by the expansion of the two HII regions marked by red circles. Pixels that do not meet the conditions for a good fit are blanked.

formed per unit time:

$$SFR(t) = \frac{\Delta M_{\star}}{\Delta t}. \quad (7)$$

On the other hand, hydrodynamic simulations give us the mass in sink particles in discrete time steps instead of continuous ones. Thus, we can only calculate a time-averaged SFR:

$$\langle SFR(t) \rangle = \frac{M_{\star}(t) - M_{\star}(t_0)}{t - t_0}. \quad (8)$$

One of the biggest problems in estimating the SFR from observations, is that calculating the total mass of newly formed stars is challenging. This can only be done in a few cases where the regions are close enough so that individual stellar objects can be counted (e.g., Evans et al. 2009; Gutermuth et al. 2009). Moreover, even in the closest star-forming regions, the youngest YSOs are deeply embedded and the calculation of their (proto)stellar masses is uncertain and depends on the modelling of the effect the emitted radiation on their envelopes (e.g., Robitaille 2017; De Buizer et al. 2017).

In an extragalactic context, the SFR is calculated using its relation with the luminosity of various tracers (for a full review of the topic see Kennicutt & Evans 2012), usually given in the form of:

$$\frac{SFR_{\lambda}}{M_{\odot} \text{yr}^{-1}} = a_{\lambda} \left(\frac{\nu L_{\nu}(\lambda)}{\text{erg s}^{-1}} \right)^b, \quad (9)$$

where $b = 1$ in almost all the cases, and a is called the calibration coefficient. Two of the most used tracers in the IR domain are the monochromatic luminosities at $24 \mu\text{m}$ (Kennicutt & Evans 2012) and $70 \mu\text{m}$ (Li et al. 2010), for which the calibration coefficients are $a_{24} = 2.03 \times 10^{-43}$ and $a_{70} = 1.7 \times 10^{-43}$ respectively. Another tracer that is commonly used is the total IR (TIR) luminosity from 8 to $1000 \mu\text{m}$ (Murphy et al. 2011), for which $a_{\text{IR}} = 3.88 \times 10^{-44}$. The SFR calculated with these estimators is sensitive to different timescales (namely different Δt in Equation 7), ranging from ~ 10 to ~ 100 Myr. Using a sample of Galactic star forming regions for which the more massive components of the

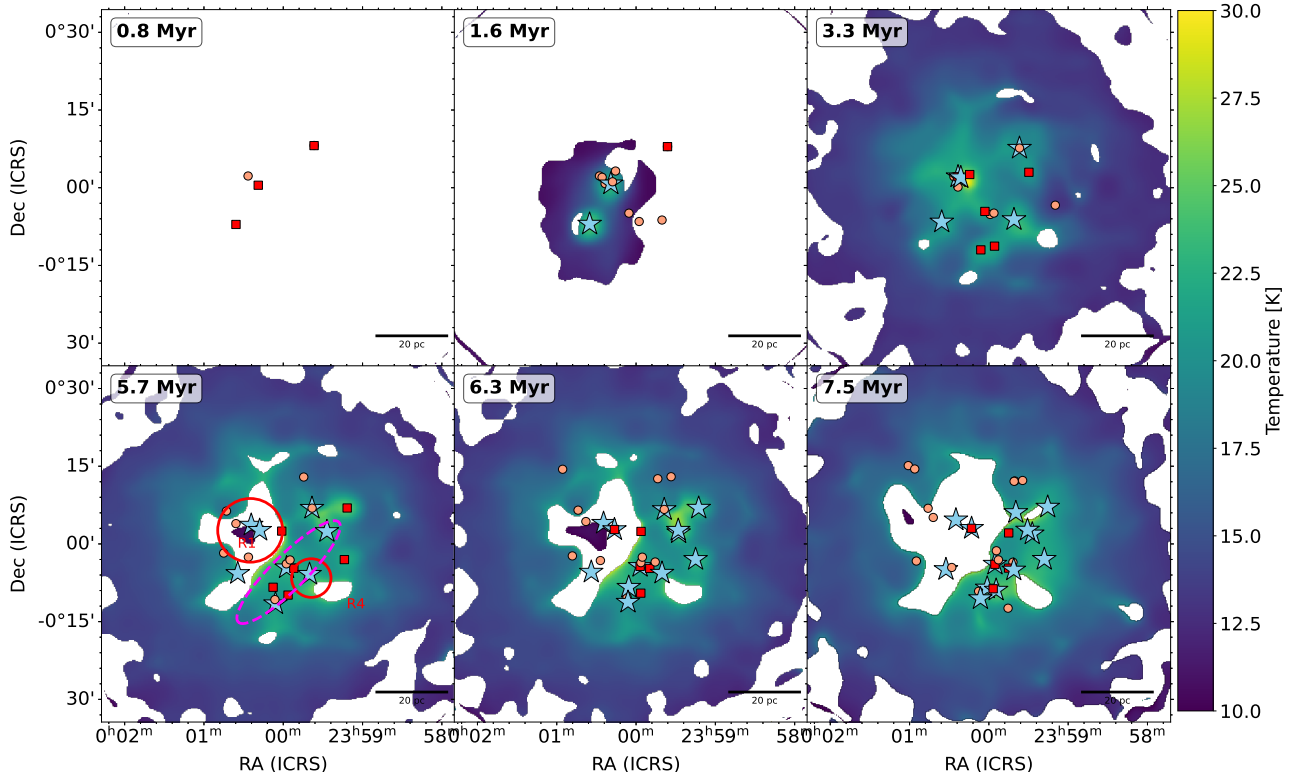


Figure 9: Dust temperature maps in Kelvin resulting from the spatially resolved fitting to the face-on synthetic observations at various timesteps. Labels and symbols are the same as in Figure 8.

stellar population could be resolved, [Binder & Povich \(2018\)](#) recalculated the values of the a_λ coefficients.

Here we perform a similar analysis, checking both how the calibration of [Binder & Povich \(2018\)](#) applies to our simulation, and calculating independently the aforementioned calibration coefficients. We note that, on the one hand, using the synthetic observations permit us to know all the intrinsic physical properties of the simulations, but on the other hand, we are only sampling one particular star forming region, and hence cannot explore the diversity of the physical properties that characterize the ensemble of regions found in galaxies. We also note that the latest snapshot of the simulation that we use is at 7.5 Myr after the onset of star formation, which is fairly similar to the time range probed by the $24 \mu\text{m}$ luminosity. On the other hand, both the $70 \mu\text{m}$ and the bolometric far-IR luminosities are sensitive to larger periods, typically ~ 100 Myr, which is significantly larger than the simulated interval.

In order to derive the coefficients as in [Binder & Povich \(2018\)](#), we first need to calculate the intrinsic SFR of the simulation. [Zamora-Avilés et al. \(2019\)](#) gives the value of mass that is locked in sinks at each snapshot,

which are separated by 0.1 Myr. From this, the SFR can be calculated in two ways: 1) the “instantaneous” SFR (hereafter iSFR), which is the difference in the mass contained in sinks between two successive simulation snapshots, and 2) the “100-Myr averaged” SFR (hereafter SFR_{100}), which is calculated using Equation 8. For this, we set the initial time to $t_0 = 92.5$ Myr before the first sink was born. Like this, [Binder & Povich \(2018\)](#) found values of $a_{24} = 3.7 \pm 2.4 \times 10^{-43}$, $a_{70} = 2.7 \pm 1.4 \times 10^{-43}$ and $a_{\text{IR}} = 1.2 \pm 0.7 \times 10^{-43}$, for the monochromatic and total IR tracers, respectively. We have used their prescriptions to calculate the predicted SFR of the simulated cloud from our synthetic observations (see Figure 10).

Conversely, we calculate the a parameters using Equation 9 and SFR_{100} as a reference, for the three tracers mentioned above from our synthetic observations. We find that the best values for the calibration coefficients, averaging the snapshots from 3.3 to 7.5 Myr and lines of sight, are $a_{24} = 4.26 \times 10^{-43}$, $a_{70} = 1.08 \times 10^{-43}$ and $a_{\text{IR}} = 8.24 \times 10^{-44}$. These values are 1.15, 0.4, and 0.69 times the values reported by [Binder & Povich \(2018\)](#) for the 24, 70, and TIR tracers.

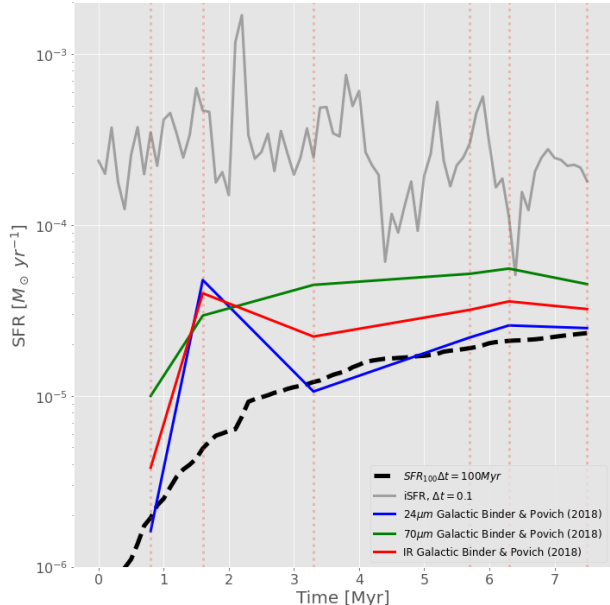


Figure 10: Predicted SFR for the simulation using the Galactic calibration from [Binder & Povich \(2018\)](#), using the monochromatic luminosities at 24 (blue line) and 70 (green line) μm . The red line shows the predicted SFR using the total IR luminosity. The intrinsic iSFR and SFR_{100} are shown as a solid gray line and dashed black line, respectively.

6. DISCUSSION

Creating synthetic observations of simulated star formation regions gives the opportunity to analyze their SED, exploiting standard techniques which are usually applied to real observations, and helping to determine possible biases and limitations of these very same techniques. Furthermore, as we have seen in the previous section, the comparison with observed data can provide important hints to the inevitable limitations carried on by numerical simulations. In this section we give further interpretation of the results presented in the previous sections.

6.1. The role of the interstellar radiation field

In contrast to other radiative transfer codes such as HYPERION ([Robitaille 2011](#)), where the dust temperature can be started at a specific baseline temperature during the radiative transfer (see for example, [Koeperl et al. 2017a,b,c](#)), in SKIRT the dust temperature is calculated self-consistently by design. Then, when considering the simulated molecular cloud as an isolated system, we found that the peak of the IR SED, especially in the first evolutionary stages, is located at shorter wavelengths with respect to similar real star forming regions.

This indicated higher dust temperatures with respect to observations for the parts of the cloud dominating the SED. For the simulated cloud these parts were the pock-

ets of gas around the few sinks formed at early times, but in real IRDCs the bulk of the luminosity comes from the extended cloud itself ([Lin et al. 2017](#)). When we analyzed the dust temperature distribution of the earlier snapshots as obtained from the spatial grid of the RT simulation, we found an average mass-weighted value of about 3.7 K, an extremely low temperature even for IRDCs. This turned out to be due to the limited stellar radiation being mostly absorbed “in situ”, and therefore not being able to reach the outer regions. This motivated us to include the ISRF as an extra source of radiation, which is effective in heating dust over the entire cloud to realistic values in the earliest snapshots equivalent to young clouds such as IRDCs. The addition of this external radiation component is physically motivated and represents a step further toward a more realistic representation of dust emission star forming clouds.

In order to assess the importance of the ISRF, we compare RT models where we only use stars as sources of radiation versus models where the ISRF is also included. Figure 11 shows the resulting SEDs and projected column densities for the snapshots at 0.8, 1.6, and 3.3 Myr. The surface density maps in Figure 11 show the presence of important relative voids of material in many lines of sight. These voids are initially formed as a consequence of molecular cloud collapse, which collects the material in filaments, leaving low-density regions around them (e.g., [Gómez & Vázquez-Semadeni 2014](#)), and at later times are also due to the expansion of HII regions ([Zamora-Avilés et al. 2019](#)). The ISRF can freely cross the cloud through these voids. In the earliest snapshot we see that the ISRF dominates the total SED from the UV up to $\sim 10 \mu\text{m}$. Thus the above mentioned effect is significant. In the following snapshot at 1.6 Myr, the ISRF direct emission is now overwhelmed by emission from the cloud itself. At this age, the stellar radiation begins to dominate dust heating, even in the outer regions of the cloud. The ISRF contributes significantly to the SED at $\sim 2 \mu\text{m}$ and $> 500 \mu\text{m}$. At 3.3 Myr the relative contribution of the ISRF to the SED is even smaller.

Finally, we note that even though the ISRF was included to pre-heat the cloud dust to realistic values prior to star formation, the effect here discussed does not affect the analysis in Section 5, because it is removed as part of the background subtraction to the create the observed synthetic SEDs.

6.2. Comparison to Galactic star-forming regions

Although the hydrodynamical simulation analyzed in this work does not attempt to reproduce any specific real region, given the physics it includes and characteristics

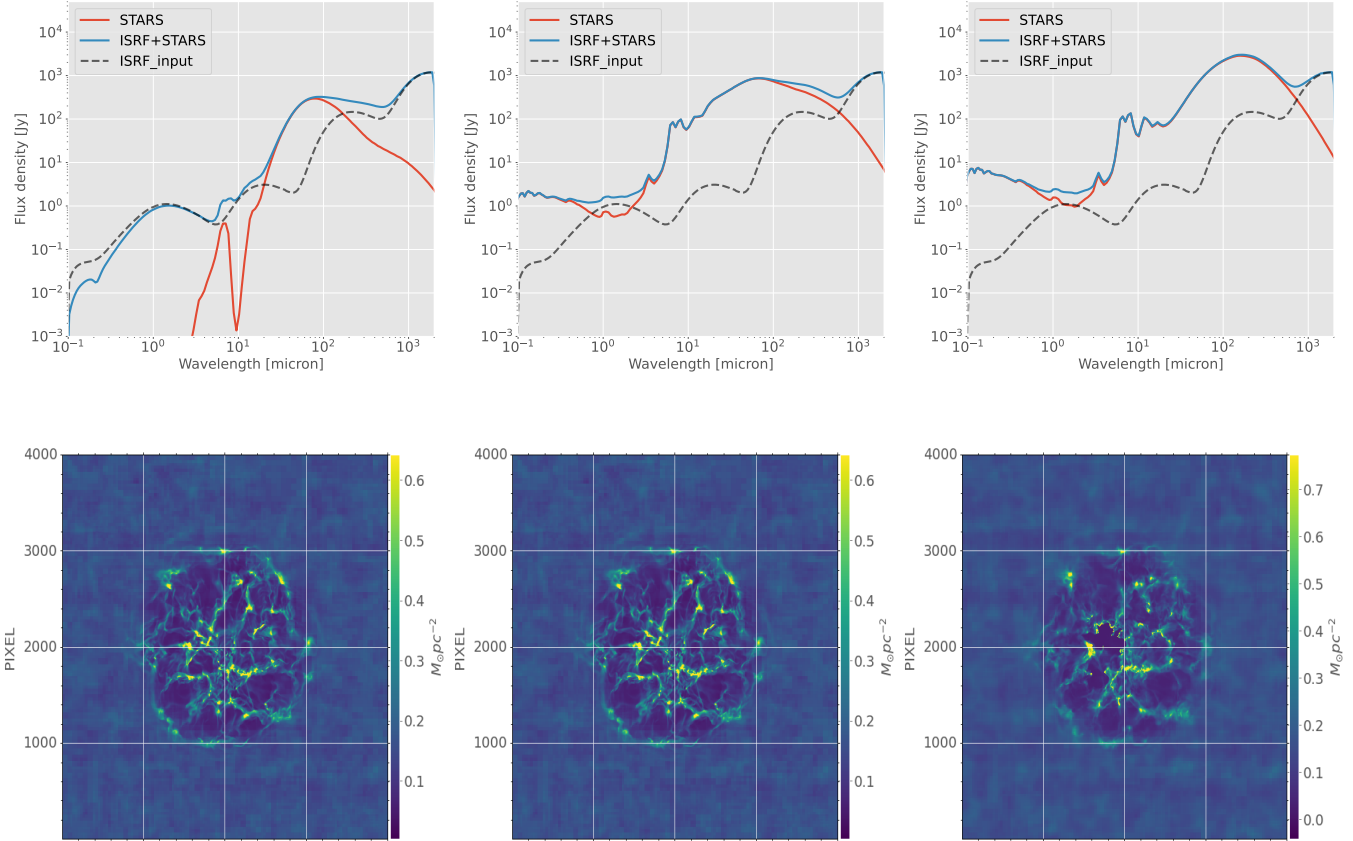


Figure 11: *Top row:* Raw SEDs for the radiative transfer models when we use only stars (red line) or add the ISRF (blue line) as sources of radiation. The black dashed line represents the input SED of the ISRF. *Bottom row:* Dust grid column-density projection of the face-on line of sight. Columns are the results of snapshots at 0.8, 1.6, 3.3 Myr.

such as surface density and filamentary clump morphology, we expect it to share similar characteristics to those of massive star-forming regions observed in the Galaxy (e.g., Liu et al. 2012; Galván-Madrid et al. 2013; Motte et al. 2022; Traficante et al. 2023).

The first snapshot does not reproduce the typical SED of young, massive star formation regions such as those in Lin et al. (2017), even after the inclusion of the ISRF. Later snapshots do enter the range where they are comparable to IRDCs and the Orion star formation region (e.g., Lada et al. 2010; Stutz 2018; Román-Zúñiga et al. 2019). Figure 5 shows this comparison with the Orion nebula SED provided in Binder & Povich (2018). However, an important caveat is that the Orion SED was measured in a radius of a few pc around the Trapezium nebula, whereas the aperture of the observed synthetic SED has a size of 100 pc. Therefore the real Orion star formation region appears to be much more concentrated than the simulated cloud. Also, in general the SEDs of our simulation peak toward longer wavelengths as compared to the sample of galactic star-forming regions.

Therefore, more realistic hydrodynamical simulations should have a similar star formation rate but over a smaller volume. This will also allow to heat dust to higher temperatures, and produce SEDs that peak at about 100 μm , as observed.

As mentioned in Section 3.1, the sink particles are populated in a stochastically-sampled way using the IMF as a probability density function, and from the different realizations we used the one that gave us the median bolometric luminosity. Since our cloud appears to be colder than the Galactic sample, we performed a radiative transfer model for the snapshot at 3.3 Myr using the realization having the maximum bolometric luminosity. This extreme model has a relative excess of massive stars, and a total input stellar luminosity of $10^7 L_{\odot}$ (see Appendix C), which is three orders of magnitude higher than the model with median luminosity (see Table 2). This extra energy produces an SED closer to the one of the W49A cloud, one of the most luminous star-formation regions in the Galaxy with $L_{\text{FIR}} > 10^7 L_{\odot}$ (Lin et al. 2016). The above result illustrates the dra-

matic effect that an excess of massive stars, either due to stochastic sampling (Orozco-Duarte et al. 2022) or an intrinsically top-heavy IMF (Schneider et al. 2018; Pouteau et al. 2022) can have in the observational appearance of molecular clouds.

6.3. Testing MBB fitting

In Section 5 we modeled the dust emission as a modified black body with a fixed emissivity index β , using both integrated and spatially resolved fluxes.

First, we used a single temperature MBB to reproduce the spatially-integrated *Herschel* observations in the 160 to 500 μm range. This model yielded a temperature averaged over the last four snapshots of 17 K, and a total dust mass of $\sim 430 M_{\odot}$ and $\sim 490 M_{\odot}$ for the face-on and edge-on views, respectively. Therefore, the model underestimated the intrinsic dust mass by about a factor $\times 2$. We also tested the MBB fitting by adding the 100 μm photometric point. This fit yielded a dust temperature of ~ 20 K, which resulted in a decrease of the dust mass by $\sim 100 M_{\odot}$ with respect to the previous fit, for both lines of sight. The MBB fits for this case tend to slightly underestimate the emission at the longer wavelengths. This suggests that assuming dust at a single temperature is not an optimal assumption, as this model would not properly represent variations in the line of sight.

Since dust properties are luminosity weighted in the line of sight, and the IR emission tends to be dominated by the warmer dust (see Section 5.3, and, e.g., Malinen, J. et al. 2011; Ysard et al. 2012), in this work we also use a 2-temperature MBB model using the six bands of *Herschel* in order to characterize both the warm and cold dust components. We found that, although the warm dust component (with temperatures of ~ 30 K) accounts for a very small fraction ($\leq 5\%$) of the total mass recovered by the fit, the addition of a second component allows the colder component to better recover the emission at longer wavelengths. Therefore, the total dust using a 2-temperature MBB is closer to the intrinsic mass of the simulation. We suggest that whenever enough data points from the mid- to the far-IR are available, the best option is use two-component models (e.g., Immer et al. 2014). While this is still a simplified approach, it seems to be the best compromise between the number of data points and number of parameters.

We also explored the consequences of performing the MBB fitting in a spatially-resolved way. This has the advantage of partially alleviating the effect of line of sight variations, at least compared to spatially-integrated fluxes. Furthermore, with this type of analysis we can follow the evolution of both the temperature and the sur-

face density in our models. From a comparison of the integrated and spatially-resolved results (see Table 4), we conclude that the latter, using a 2-temperature MBB, is the one that recovers a total mass closer ($\sim 66\%$) to the intrinsic dust mass in the simulation grid.

As we mentioned in Section 6.1, SKIRT calculates the dust temperature self-consistently, and we can not define a base temperature for the dust prior to the radiative transfer simulation. In an analysis similar to ours, Koepferl et al. (2017a) found that in their model without background, in which they couple the dust temperature to an isothermal field at $T_{\text{iso}} = 18$ K, the total mass recovered in their pixel-by-pixel analysis is very close to the intrinsic mass in their simulations. The median ratio and median absolute deviation of their recovered to intrinsic column densities is 1.12 ± 0.28 . In our case, for the face-on line of sight, we find a ratio and deviation of 0.58 ± 0.12 for the resolved, single-component MBB fitting, and 0.66 ± 0.13 for the case of two-component MBBs, also in a resolved way. Both values are averaged over the last four snapshots.

We further explored the fact that in the spatially resolved analysis the calculated total mass is closer to the intrinsic mass, but still underestimated. We performed a test in which we reduce the size of the analysis box M_{100pc} in the x-axis from 100 to 30 pc, or about the size of densest part of the cloud in this axis (see Figure 14). The total mass inside this new box, averaged in the last four snapshots, is $563 M_{\odot}$. For the case of this reduced box, the ratio of the dust mass recovered by resolved 2-temperature MBB fitting is ~ 1.04 times the intrinsic one. This proves that the origin of the “missing mass” is that our analysis does not recover the coldest dust in the simulation grid.

6.4. SFR

Individual star forming regions are in general characterized by different stellar contents and SFR values, this being due to their different initial conditions and evolutionary stage (e.g., Lada et al. 2010; Binder & Povich 2018; Motte et al. 2022).

We now check how the SFR varies among different parts of our simulated cloud, and how this broadly compares with values observed in actual massive star formation regions. The SFR value calculated from different tracers, in our case, monochromatic and total IR luminosities, will generally depend on the evolutionary stage of the cloud, and on where this luminosity is measured. We calculated SFRs using the calibration coefficients a found in Section 5.5, using apertures of different sizes centered in two sub-regions. These sub-regions represent contrasting scenarios in the 3.3 Myr snapshot. The first

one, region A, is centered on the massive star-forming region which has an HII region in expansion (R1 in Fig. 8). The second, region B, is centered on a young star-forming region that appears as an over-density at 5.7 Myr (magenta ellipse in Figure 8).

In Figure 12 we plot the SFRs for a Galactic sample, whose data have been taken with apertures of different sizes (Binder & Povich 2018), along with the SFRs for our synthetic observations. We use apertures of 10, 20, 30, and 50 pc, at 3.3 Myr, 5.7 Myr, and 7.6 Myr. We consider the monochromatic 24 and 70 μm , and the total IR luminosity. The constants a that we use are those averaged over 100 Myr. It is seen that, for a given aperture radius, the inferred SFRs for the simulation are systematically smaller than in observations. This again suggests that star formation in the simulated cloud is more scattered than in real clouds.

Unsurprisingly, SFRs calculated at all radii for region A are generally smaller than those calculated for region B. This is because region A is progressively getting depleted from dust due to ionization feedback. In contrast, in region B the amount of dust is steadily increasing due to the concurrent action of the nearby HII regions, which trigger star formation at this location.

The 24 μm tracer is the one that suffers larger changes due to both the evolutionary stage of the region and, to some degree, the aperture size. This is likely due to the fact that at this wavelength the emission is dominated by the warmer dust which is located closer to the young stars, and that this brighter, warmer dust occupies a smaller volume compared to the colder dust. Therefore its spatial configuration and resulting flux evolves faster in time. As for the 70 μm and total IR tracers, there is only a weak dependence of the SFR as a function of the aperture used for the flux measurement. Furthermore, the value calculated using these two tracers shows almost no differences as a function of time, with the only exception of the one calculated in the smaller region of the 5.7 Myr snapshot. Note also that for the smallest aperture centered in region A, the inferred SFR is very small, thus is not shown in Figure 12.

7. CONCLUSIONS

In this work we have presented and analyzed post-processing Monte Carlo dust radiative transfer, made with SKIRT, of the hydrodynamical simulation with ionizing feedback presented by Zamora-Avilés et al. (2019), which was created in the context of the global hierarchical collapse scenario (Vázquez-Semadeni et al. 2019). The synthetic observations were analyzed using common observational techniques, including photome-

try and morphological analysis, as well as integrated and resolved SED fitting.

A crucial ingredient in the creation of the synthetic observations is the choice of the primary sources of photons. To consider the effects of stochasticity in the stellar populations that are represented by sink particles, we sampled each of them with many realizations of an IMF and selected those with the median luminosity. The effects of a different selection were explored and can be dramatic. Another key aspect was the inclusion of a prescription for the interstellar radiation field, which allowed to pre-heat the dust over the entire cloud to realistic levels prior to significant star formation.

The infrared appearance of the simulated cloud evolves from a quiescent region, analogous to IRDCs, to active star formation with the presence of bubbles and ridges caused by the expansion of HII regions. This evolution occurs over a total interval of about 8 Myr after the onset of star formation, but the global IR SED settles rather quickly after 3 Myr. The final luminosity of the cloud is comparable to that of the Orion nebula cluster, but spread over a much larger area.

We used the synthetic observations to test the effectiveness of standard techniques to recover properties such as dust mass and temperature. We performed modified black body fitting with one and two temperature components, both in the spatially-integrated SEDs and in a resolved fashion. MBB fitting systematically underestimates the intrinsic dust mass in the simulation grid by about a factor $\times 2$. Pixel-by-pixel fitting recovers about 70% of the dust mass. The “missing mass” consists of the coldest dust with temperatures significantly below 10 to 15 K, whose thermal emission does not contribute to the flux of the cloud, even at far-IR wavelengths. We believe that this effect is real and could affect observations, insofar clouds have some very cold dust.

Finally, we tested observational calibrations of the global star formation rate of the cloud based on monochromatic fluxes at 24 and 70 μm , as well as total IR emission, obtaining results consistent with observations of a Milky Way sample reported by Binder & Povich (2018). However, the star formation rate in the simulated cloud – as mentioned before for the case of the luminosity – appears to be less concentrated than in observed star forming clouds. This suggests that the prescription for the assembly mechanism responsible for cloud formation and evolution in the simulation is not capable of bringing enough gas into a small enough region. Future simulations within the GHC scenario will explore this issue, which likely requires further gravitational focusing from even larger scales.

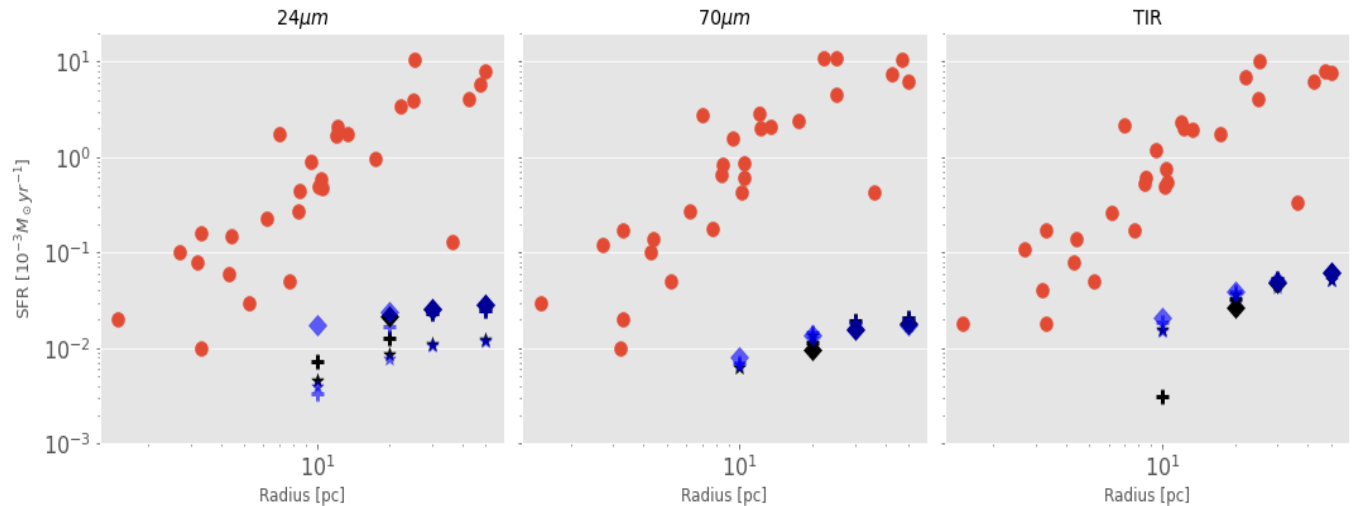


Figure 12: SFR plotted versus aperture size of the observation. The red dots represent SFR values taken from the Binder & Povich (2018) sample. The other symbols represent the inferred SFRs for simulation snapshots: \star = 3.3 Myr, $+$ = 5.7 Myr, and \diamond = 7.6 Myr. Black symbols represent the synthetic observations of region A (HII region). Blue symbols represent region B (younger, triggered star formation).

Regarding the comparison of simulations to observations, a step forward from the work presented in this paper will be to analyze a sample of simulated clouds spanning the relevant range of formation mechanisms and physical conditions known to exist in molecular clouds. Ideally, the simulated clouds should form self-consistently from larger (galactic) scales (e.g., Walch et al. 2015; Smith et al. 2020), and include realistic prescriptions for their turbulence and magnetic fields. Also, the relevant sources of stellar feedback (HII regions, radiation pressure onto dust, stellar winds, bipolar outflows) should ideally be included. Recent efforts toward that direction have been presented by Grudić et al. (2022). This is a challenging issue, and typically simulations are only able to include some but not all of these processes (e.g., Peters et al. 2011; Krumholz et al. 2012; Dale et al. 2014). We plan to present further work on the comparison of synthetic and real observations in the future.

ACKNOWLEDGMENTS

JJD and RGM acknowledge support from UNAM-PAPIIT project IN108822, and from CONACyT Ciencia de Frontera project ID: 86372. RGM also acknowledges support from the AAS Chrétien International Research Grant. JJD and JF acknowledge support from UNAM-PAPIIT project IN111620. The authors thank the anonymous referee for a timely and useful report.

Software: `astropy` (Astropy Collaboration et al. 2022), `SKIRT` (Camps & Baes 2015, 2020), `LMFIT` (Newville et al. 2021), `IMF` (<https://github.com/keflavich/imf>)

APPENDIX

A. EXAMPLE FLAT SED FITTING

As pointed out in Section 5.4, in the two youngest snapshots of the simulation, dust emission in some pixels is not adequately modelled by a single modified black body. Figure 13 shows a representative example.

B. SYNTHETIC EVOLUTION IN EDGE-ON VIEW

Here we show the evolution of the recovered dust surface density (Figure 14) and temperature (15) when the simulated cloud is viewed from an edge-on orientation.

C. EXPLORING THE EFFECT OF AN EXCESS OF MASSIVE STARS

In the building of the input SEDs for each sink, we have explored about 200 different ways to distribute the total sink mass into individual stars, using a stochastic sampling of the Kroupa IMF. Then, we have calculated the bolometric

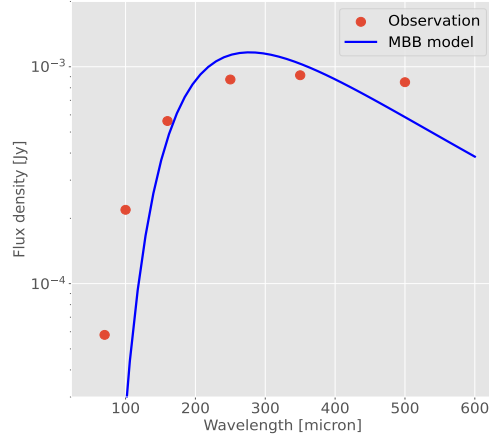


Figure 13: Representative SED of a pixel with a poor fit in the first two timesteps of Figure 8. The blue line represents the MBB emission with the temperature and mass that best fit the observed fluxes (red dots). The flat SED observed at the two earlier snapshots was already discussed for the integrated SEDs in section 5.1, and is also seen at the pixel scale.

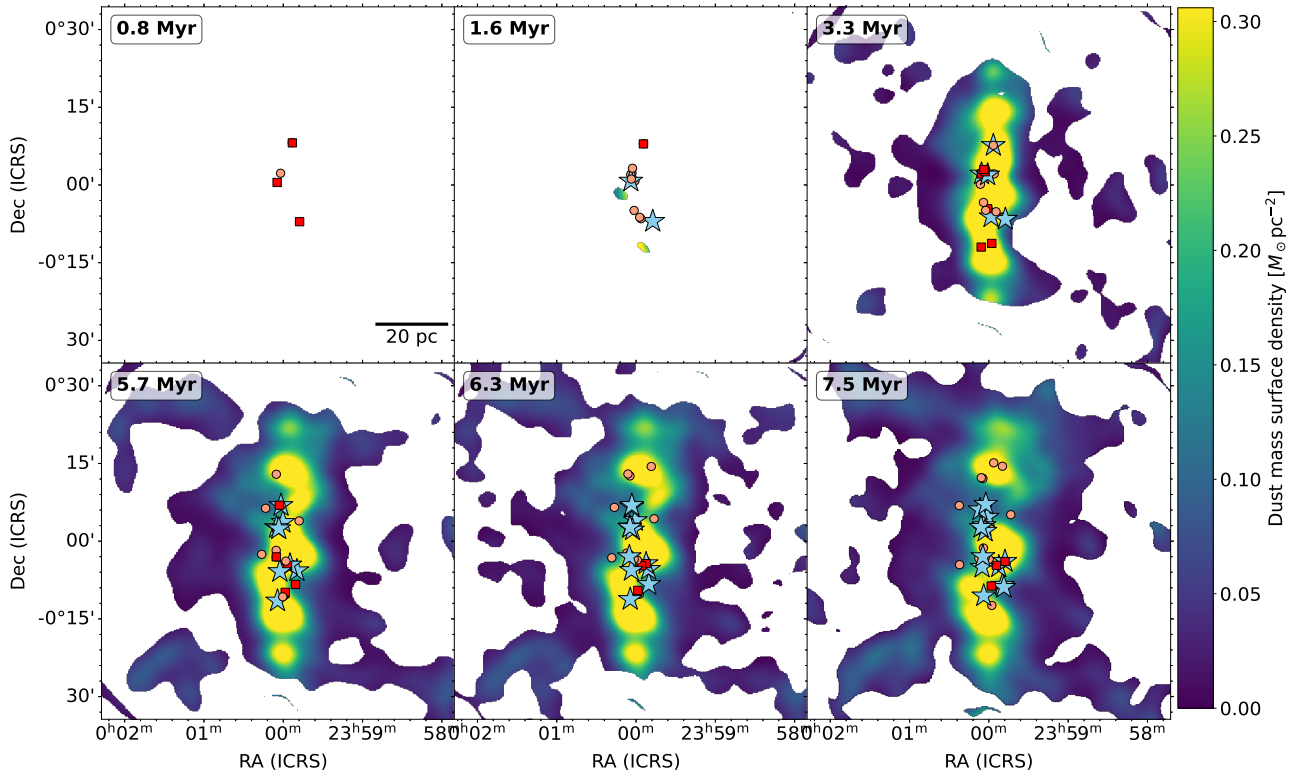


Figure 14: Dust surface density maps ($M_{\odot} \text{pc}^{-2}$) resulting from the spatially resolved fitting to the edge-on synthetic observations at various timesteps. The markers represent the projected sink positions, in blue stars for the sinks with masses $\geq 100 M_{\odot}$, in red squares for sinks with masses between $50 M_{\odot}$ and $100 M_{\odot}$, and in orange circles the sinks with $\leq 50 M_{\odot}$.

luminosity for each of these realizations, and we have used as input spectra for the sinks the ones with median luminosity. In this appendix, we test the effects of taking the spectra with the maximum luminosity, which contain

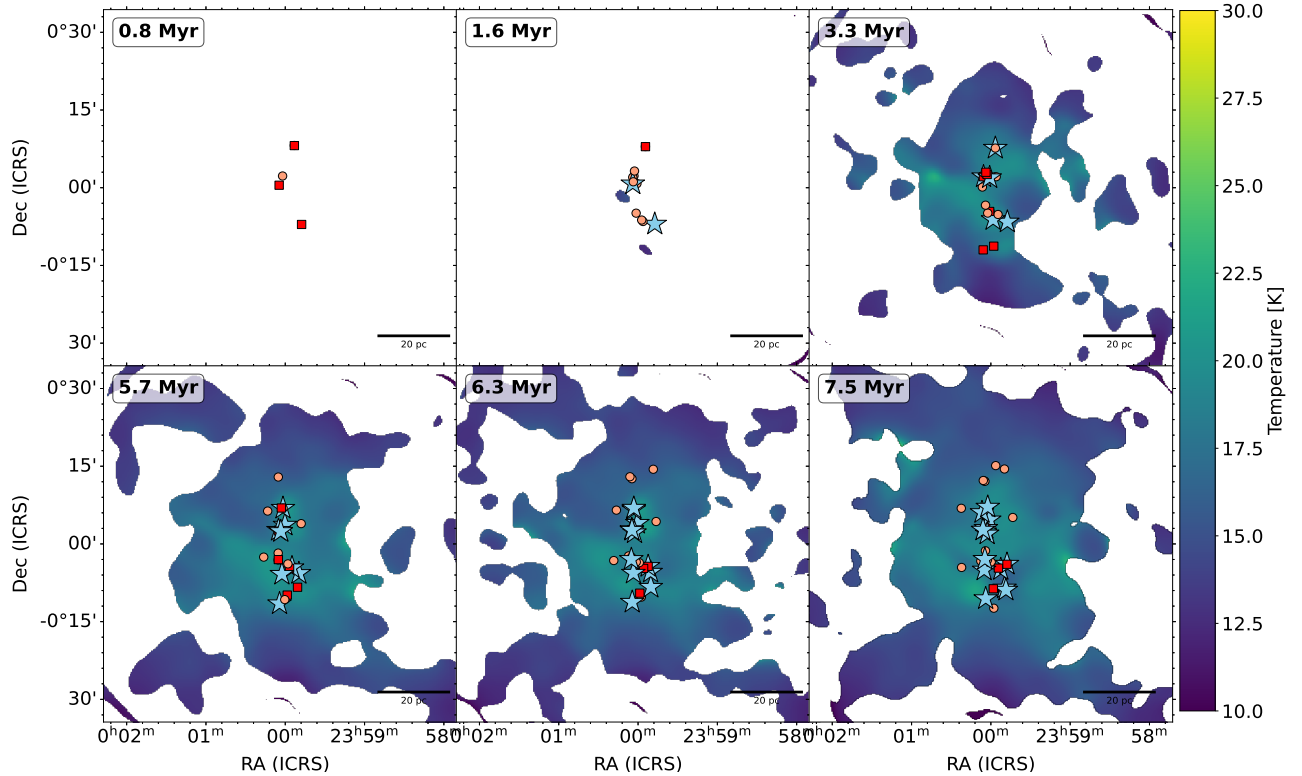


Figure 15: Dust temperature maps in Kelvin resulting from the spatially resolved fitting to the edge-on synthetic observations at various timesteps. Labels and symbols are the same as in Figure 14.

more massive stars with respect to the ones with the median luminosity. An excess of massive stars could be obtained due to real stochasticity in the forming cluster, or by an intrinsically top-heavy stellar IMF.

Figure 16 shows the number of massive ($M > 8 M_{\odot}$) stars for each snapshot and for three different realizations of the stochastic IMF sampling: minimum, median, and maximum luminosity. In Figure 17 we compare the SEDs of the face-on, median-luminosity models (also shown in Figure 5) with those of maximum luminosity. We performed this test for the snapshots at 3.3, 5.7, and 6.3 Myr. One of the most notable differences, in addition to the much larger luminosities, is that the peak of the SED is displaced to shorter ($\sim 70 \mu\text{m}$) wavelengths.

REFERENCES

- Aguirre, J. E., Ginsburg, A. G., Dunham, M. K., et al. 2011, *ApJS*, 192, 4, doi: [10.1088/0067-0049/192/1/4](https://doi.org/10.1088/0067-0049/192/1/4)
- Alves de Oliveira, C., Schneider, N., Merín, B., et al. 2014, *A&A*, 568, A98, doi: [10.1051/0004-6361/201423504](https://doi.org/10.1051/0004-6361/201423504)
- Anderson, L. D., Bania, T. M., Balsa, D. S., et al. 2014, *ApJS*, 212, 1, doi: [10.1088/0067-0049/212/1/1](https://doi.org/10.1088/0067-0049/212/1/1)
- Arthur, S. J., Henney, W. J., Mellema, G., de Colle, F., & Vázquez-Semadeni, E. 2011, *MNRAS*, 414, 1747, doi: [10.1111/j.1365-2966.2011.18507.x](https://doi.org/10.1111/j.1365-2966.2011.18507.x)
- Astropy Collaboration, Price-Whelan, A. M., Lim, P. L., et al. 2022, *apj*, 935, 167, doi: [10.3847/1538-4357/ac7c74](https://doi.org/10.3847/1538-4357/ac7c74)
- Battersby, C., Ginsburg, A., Bally, J., et al. 2014, *ApJ*, 787, 113, doi: [10.1088/0004-637X/787/2/113](https://doi.org/10.1088/0004-637X/787/2/113)
- Beck, R. 2001, *SSRv*, 99, 243
- Betti, S. K., Gutermuth, R., Offner, S., et al. 2021, *ApJ*, 923, 25, doi: [10.3847/1538-4357/ac2666](https://doi.org/10.3847/1538-4357/ac2666)
- Binder, B. A., & Povich, M. S. 2018, *The Astrophysical Journal*, 864, 136
- Bressan, A., Marigo, P., Girardi, L., et al. 2012, *Monthly Notices of the Royal Astronomical Society*, 427, 127, doi: [10.1111/j.1365-2966.2012.21948.x](https://doi.org/10.1111/j.1365-2966.2012.21948.x)

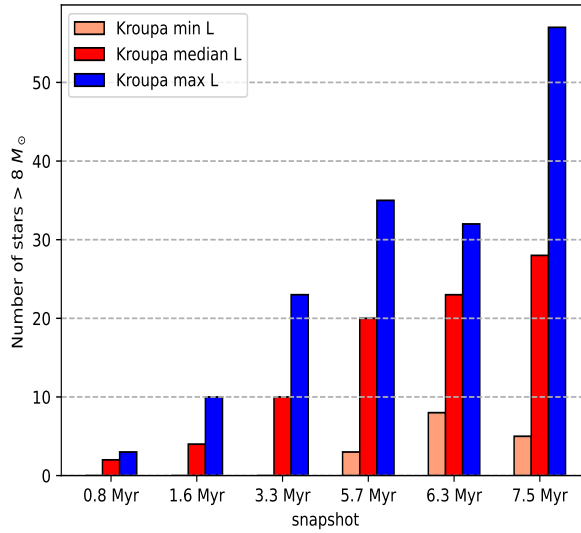


Figure 16: Histogram of the total number of stars with masses higher than $8 M_{\odot}$, for the minimum, median, and maximum luminosity realizations resulting from the IMF stochastic sampling.

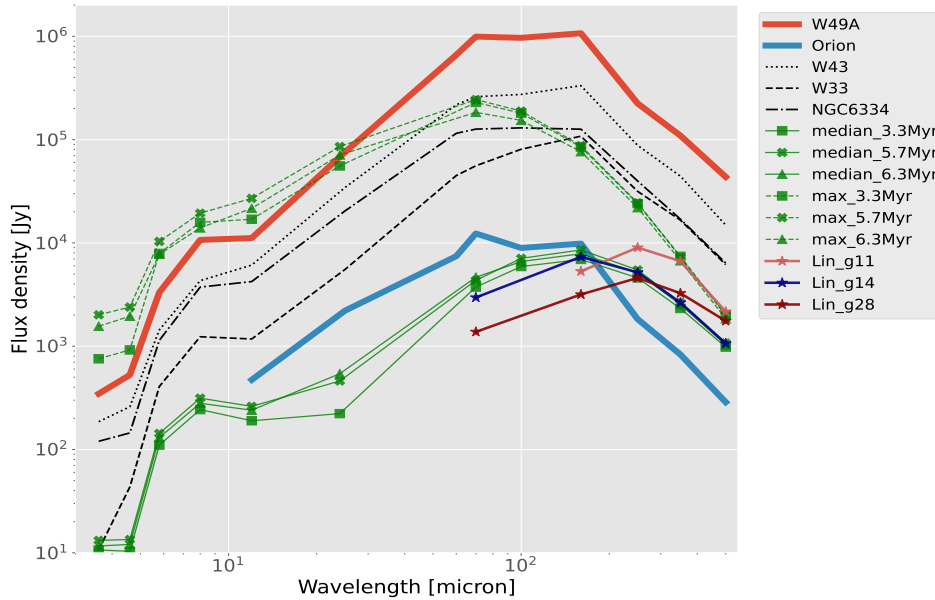


Figure 17: Similar to Figure 5, but the median-luminosity models are only plotted for the snapshots at 3.3, 5.7, and 6.3 Myr (face-on, solid green lines). The corresponding maximum-luminosity models are plotted with green dashed lines.

Bruzual, G. 2010, *Philosophical Transactions of the Royal Society of London Series A*, 368, 783,

doi: [10.1098/rsta.2009.0258](https://doi.org/10.1098/rsta.2009.0258)

Bruzual, G., & Charlot, S. 2003, *MNRAS*, 344, 1000

Camps, P., & Baes, M. 2015, *Astronomy and Computing*, 9, 20

—. 2020, *Astronomy and Computing*, 31, 100381

Camps, P., Kapoor, A. U., Trcka, A., et al. 2022, *MNRAS*, 512, 2728, doi: [10.1093/mnras/stac719](https://doi.org/10.1093/mnras/stac719)

Camps, P., Trayford, J. W., Baes, M., et al. 2016, *MNRAS*, 462, 1057, doi: [10.1093/mnras/stw1735](https://doi.org/10.1093/mnras/stw1735)

Chevance, M., Kruijssen, J. M. D., Vazquez-Semadeni, E., et al. 2020, *SSRv*, 216, 50, doi: [10.1007/s11214-020-00674-x](https://doi.org/10.1007/s11214-020-00674-x)

Churchwell, E., Babler, B. L., Meade, M. R., et al. 2009, *PASP*, 121, 213, doi: [10.1086/597811](https://doi.org/10.1086/597811)

Colín, P., Vázquez-Semadeni, E., & Gómez, G. C. 2013, *MNRAS*, 435, 1701, doi: [10.1093/mnras/stt1409](https://doi.org/10.1093/mnras/stt1409)

- Commerçon, B., Hennebelle, P., & Henning, T. 2011, *ApJL*, 742, L9, doi: [10.1088/2041-8205/742/1/L9](https://doi.org/10.1088/2041-8205/742/1/L9)
- Da Rio, N., Tan, J. C., & Jaehnig, K. 2014, *ApJ*, 795, 55, doi: [10.1088/0004-637X/795/1/55](https://doi.org/10.1088/0004-637X/795/1/55)
- Dale, J. E., Ercolano, B., & Bonnell, I. A. 2012, *MNRAS*, 424, 377, doi: [10.1111/j.1365-2966.2012.21205.x](https://doi.org/10.1111/j.1365-2966.2012.21205.x)
- Dale, J. E., Ngoumou, J., Ercolano, B., & Bonnell, I. A. 2014, *MNRAS*, 442, 694, doi: [10.1093/mnras/stu816](https://doi.org/10.1093/mnras/stu816)
- De Buizer, J. M., Liu, M., Tan, J. C., et al. 2017, *ApJ*, 843, 33, doi: [10.3847/1538-4357/aa74c8](https://doi.org/10.3847/1538-4357/aa74c8)
- De Looze, I., Fritz, J., Baes, M., et al. 2014, *Astronomy & Astrophysics*, 571, A69
- Deharveng, L., Schuller, F., Anderson, L. D., et al. 2010, *A&A*, 523, A6, doi: [10.1051/0004-6361/201014422](https://doi.org/10.1051/0004-6361/201014422)
- Deharveng, L., Zavagno, A., Anderson, L. D., et al. 2012, *A&A*, 546, A74, doi: [10.1051/0004-6361/201219131](https://doi.org/10.1051/0004-6361/201219131)
- Draine, B., & Li, A. 2007, *The Astrophysical Journal*, 657, 810
- Draine, B. T. 1978, *The Astrophysical Journal Supplement Series*, 36, 595
- Draine, B. T. 2011, *Physics of the Interstellar and Intergalactic Medium* (Princeton University Press)
- Elagali, A., Lagos, C. D. P., Wong, O. I., et al. 2018, *MNRAS*, 481, 2951, doi: [10.1093/mnras/sty2462](https://doi.org/10.1093/mnras/sty2462)
- Evans, Neal J., I., Dunham, M. M., Jørgensen, J. K., et al. 2009, *ApJS*, 181, 321, doi: [10.1088/0067-0049/181/2/321](https://doi.org/10.1088/0067-0049/181/2/321)
- Federrath, C., & Klessen, R. S. 2012, *ApJ*, 761, 156, doi: [10.1088/0004-637X/761/2/156](https://doi.org/10.1088/0004-637X/761/2/156)
- Forbrich, J., Lada, C. J., Muench, A. A., Alves, J., & Lombardi, M. 2009, *ApJ*, 704, 292, doi: [10.1088/0004-637X/704/1/29210.48550/arXiv.0908.4086](https://doi.org/10.1088/0004-637X/704/1/29210.48550/arXiv.0908.4086)
- Fryxell, B., Olson, K., Ricker, P., et al. 2000, *The Astrophysical Journal Supplement Series*, 131, 273, doi: [10.1086/317361](https://doi.org/10.1086/317361)
- Galván-Madrid, R., Liu, H., Zhang, Z.-Y., et al. 2013, *The Astrophysical Journal*, 779, 121
- Geen, S., Bieri, R., Rosdahl, J., & de Koter, A. 2021, *MNRAS*, 501, 1352, doi: [10.1093/mnras/staa3705](https://doi.org/10.1093/mnras/staa3705)
- Ginsburg, A., Goss, W. M., Goddi, C., et al. 2016, *A&A*, 595, A27, doi: [10.1051/0004-6361/201628318](https://doi.org/10.1051/0004-6361/201628318)
- Gómez, G. C., & Vázquez-Semadeni, E. 2014, *ApJ*, 791, 124, doi: [10.1088/0004-637X/791/2/124](https://doi.org/10.1088/0004-637X/791/2/124)
- Grudić, M. Y., Guszejnov, D., Offner, S. S. R., et al. 2022, *MNRAS*, 512, 216, doi: [10.1093/mnras/stac526](https://doi.org/10.1093/mnras/stac526)
- Gutermuth, R. A., Megeath, S. T., Myers, P. C., et al. 2009, *ApJS*, 184, 18, doi: [10.1088/0067-0049/184/1/18](https://doi.org/10.1088/0067-0049/184/1/18)
- Haid, S., Walch, S., Seifried, D., et al. 2019, *MNRAS*, 482, 4062, doi: [10.1093/mnras/sty2938](https://doi.org/10.1093/mnras/sty2938)
- Haworth, T. J., Glover, S. C. O., Koepferl, C. M., Bisbas, T. G., & Dale, J. E. 2018, *NewAR*, 82, 1, doi: [10.1016/j.newar.2018.06.00110.48550/arXiv.1711.05275](https://doi.org/10.1016/j.newar.2018.06.00110.48550/arXiv.1711.05275)
- Heitsch, F., & Hartmann, L. 2008, *ApJ*, 689, 290, doi: [10.1086/592491](https://doi.org/10.1086/592491)
- Hennebelle, P., Lebreuilly, U., Colman, T., et al. 2022, *A&A*, 668, A147, doi: [10.1051/0004-6361/202243803](https://doi.org/10.1051/0004-6361/202243803)
- Hocuk, S., Szűcs, L., Caselli, P., et al. 2017, *Astronomy & Astrophysics*, 604, A58
- Hosokawa, T., & Omukai, K. 2009, *ApJ*, 691, 823, doi: [10.1088/0004-637X/691/1/823](https://doi.org/10.1088/0004-637X/691/1/823)
- Ibáñez-Mejía, J. C., Mac Low, M.-M., Klessen, R. S., & Baczynski, C. 2016, *ApJ*, 824, 41, doi: [10.3847/0004-637X/824/1/41](https://doi.org/10.3847/0004-637X/824/1/41)
- Immer, K., Galván-Madrid, R., König, C., Liu, H. B., & Menten, K. M. 2014, *A&A*, 572, A63, doi: [10.1051/0004-6361/201423780](https://doi.org/10.1051/0004-6361/201423780)
- Izquierdo, A. F., Smith, R. J., Glover, S. C. O., et al. 2021, *MNRAS*, 500, 5268, doi: [10.1093/mnras/staa3470](https://doi.org/10.1093/mnras/staa3470)
- Kalcheva, I. E., Hoare, M. G., Urquhart, J. S., et al. 2018, *A&A*, 615, A103, doi: [10.1051/0004-6361/201832734](https://doi.org/10.1051/0004-6361/201832734)
- Kennicutt, R. C., & Evans, N. J. 2012, *ARA&A*, 50, 531, doi: [10.1146/annurev-astro-081811-125610](https://doi.org/10.1146/annurev-astro-081811-125610)
- Koepferl, C. M., Robitaille, T. P., & Dale, J. E. 2017a, *The Astrophysical Journal Supplement Series*, 233, 1, doi: [10.3847/1538-4365/233/1/1](https://doi.org/10.3847/1538-4365/233/1/1)
- . 2017b, *The Astrophysical Journal*, 849, 1, doi: [10.3847/1538-4357/849/1/1](https://doi.org/10.3847/1538-4357/849/1/1)
- . 2017c, *The Astrophysical Journal*, 849, 2, doi: [10.3847/1538-4357/849/1/2](https://doi.org/10.3847/1538-4357/849/1/2)
- Kroupa, P. 2001, *MNRAS*, 322, 231
- Krumholz, M. R., Dekel, A., & McKee, C. F. 2012, *ApJ*, 745, 69, doi: [10.1088/0004-637X/745/1/69](https://doi.org/10.1088/0004-637X/745/1/69)
- Lada, C. J., Lombardi, M., & Alves, J. F. 2010, *The Astrophysical Journal*, 724, 687
- Ladjelate, B., André, Ph., Könyves, V., et al. 2020, *A&A*, 638, A74, doi: [10.1051/0004-6361/201936442](https://doi.org/10.1051/0004-6361/201936442)
- Li, Y., Calzetti, D., Kennicutt, R. C., et al. 2010, *ApJ*, 725, 677, doi: [10.1088/0004-637X/725/1/677](https://doi.org/10.1088/0004-637X/725/1/677)
- Lin, Y., Liu, H. B., Li, D., et al. 2016, *ApJ*, 828, 32, doi: [10.3847/0004-637X/828/1/3210.48550/arXiv.1606.07645](https://doi.org/10.3847/0004-637X/828/1/3210.48550/arXiv.1606.07645)
- Lin, Y., Liu, H. B., Dale, J. E., et al. 2017, *The Astrophysical Journal*, 840, 22
- Liu, H. B. 2017, *A&A*, 597, A70, doi: [10.1051/0004-6361/201629582](https://doi.org/10.1051/0004-6361/201629582)
- Liu, H. B., Jiménez-Serra, I., Ho, P. T. P., et al. 2012, *ApJ*, 756, 10, doi: [10.1088/0004-637X/756/1/1010.48550/arXiv.1206.1907](https://doi.org/10.1088/0004-637X/756/1/1010.48550/arXiv.1206.1907)
- Liu, J., Zhang, Q., Commerçon, B., et al. 2021, *ApJ*, 919, 79, doi: [10.3847/1538-4357/ac0cec](https://doi.org/10.3847/1538-4357/ac0cec)

- Louvet, F., Motte, F., Hennebelle, P., et al. 2014, *A&A*, 570, A15, doi: [10.1051/0004-6361/20142360310.48550/arXiv.1404.4843](https://doi.org/10.1051/0004-6361/20142360310.48550/arXiv.1404.4843)
- Mac Low, M.-M., & Klessen, R. S. 2004, *Reviews of Modern Physics*, 76, 125, doi: [10.1103/RevModPhys.76.125](https://doi.org/10.1103/RevModPhys.76.125)
- Malinen, J., Juvela, M., Collins, D. C., Lunttila, T., & Padoan, P. 2011, *A&A*, 530, A101, doi: [10.1051/0004-6361/201015767](https://doi.org/10.1051/0004-6361/201015767)
- Matzner, C. D. 2002, *ApJ*, 566, 302, doi: [10.1086/338030](https://doi.org/10.1086/338030)
- Molinari, S., Swinyard, B., Bally, J., et al. 2010, *A&A*, 518, L100, doi: [10.1051/0004-6361/201014659](https://doi.org/10.1051/0004-6361/201014659)
- Motte, F., Bontemps, S., & Louvet, F. 2018, *ARA&A*, 56, 41, doi: [10.1146/annurev-astro-091916-05523510.48550/arXiv.1706.00118](https://doi.org/10.1146/annurev-astro-091916-05523510.48550/arXiv.1706.00118)
- Motte, F., Bontemps, S., Csengeri, T., et al. 2022, *A&A*, 662, A8, doi: [10.1051/0004-6361/202141677](https://doi.org/10.1051/0004-6361/202141677)
- Murphy, E. J., Condon, J. J., Schinnerer, E., et al. 2011, *ApJ*, 737, 67, doi: [10.1088/0004-637X/737/2/67](https://doi.org/10.1088/0004-637X/737/2/67)
- Nanni, L., Thomas, D., Trayford, J., et al. 2022, *MNRAS*, 515, 320, doi: [10.1093/mnras/stac1531](https://doi.org/10.1093/mnras/stac1531)
- Newville, M., Otten, R., Nelson, A., et al. 2021, *lmfit/lmfit-py: 1.0.3, 1.0.3*, Zenodo, doi: [10.5281/zenodo.5570790](https://doi.org/10.5281/zenodo.5570790)
- Olivier, G. M., Lopez, L. A., Rosen, A. L., et al. 2021, *ApJ*, 908, 68, doi: [10.3847/1538-4357/abd24a](https://doi.org/10.3847/1538-4357/abd24a)
- Orozco-Duarte, R., Wofford, A., Vidal-García, A., et al. 2022, *MNRAS*, 509, 522, doi: [10.1093/mnras/stab2988](https://doi.org/10.1093/mnras/stab2988)
- Parsotan, T., Cochrane, R. K., Hayward, C. C., et al. 2021, *MNRAS*, 501, 1591, doi: [10.1093/mnras/staa3765](https://doi.org/10.1093/mnras/staa3765)
- Peters, T., Banerjee, R., Klessen, R. S., & Mac Low, M.-M. 2011, *ApJ*, 729, 72, doi: [10.1088/0004-637X/729/1/72](https://doi.org/10.1088/0004-637X/729/1/72)
- Peters, T., Banerjee, R., Klessen, R. S., et al. 2010, *ApJ*, 711, 1017, doi: [10.1088/0004-637X/711/2/101710.48550/arXiv.1001.2470](https://doi.org/10.1088/0004-637X/711/2/101710.48550/arXiv.1001.2470)
- Pillai, T., Kauffmann, J., Wyrowski, F., et al. 2011, *A&A*, 530, A118, doi: [10.1051/0004-6361/201015899](https://doi.org/10.1051/0004-6361/201015899)
- Plat, A., Charlot, S., Bruzual, G., et al. 2019, *MNRAS*, 490, 978, doi: [10.1093/mnras/stz2616](https://doi.org/10.1093/mnras/stz2616)
- Potdar, A., Das, S. R., Issac, N., et al. 2022, *MNRAS*, 510, 658, doi: [10.1093/mnras/stab3479](https://doi.org/10.1093/mnras/stab3479)
- Pouteau, Y., Motte, F., Nony, T., et al. 2022, *A&A*, 664, A26, doi: [10.1051/0004-6361/202142951](https://doi.org/10.1051/0004-6361/202142951)
- Rathborne, J. M., Jackson, J. M., & Simon, R. 2006, *ApJ*, 641, 389, doi: [10.1086/500423](https://doi.org/10.1086/500423)
- Reid, M. J., Menten, K. M., Brunthaler, A., et al. 2014, *ApJ*, 783, 130, doi: [10.1088/0004-637X/783/2/130](https://doi.org/10.1088/0004-637X/783/2/130)
- Reissl, S., Stil, J. M., Chen, E., et al. 2020, *A&A*, 642, A201, doi: [10.1051/0004-6361/202037690](https://doi.org/10.1051/0004-6361/202037690)
- Rijkhorst, E. J., Plewa, T., Dubey, A., & Mellema, G. 2006, *A&A*, 452, 907, doi: [10.1051/0004-6361:20053401](https://doi.org/10.1051/0004-6361:20053401)
- Robitaille, T. P. 2011, *A&A*, 536, A79, doi: [10.1051/0004-6361/201117150](https://doi.org/10.1051/0004-6361/201117150)
- . 2017, *A&A*, 600, A11, doi: [10.1051/0004-6361/201425486](https://doi.org/10.1051/0004-6361/201425486)
- Román-Zúñiga, C. G., Alfaro, E., Palau, A., et al. 2019, *MNRAS*, 489, 4429, doi: [10.1093/mnras/stz2355](https://doi.org/10.1093/mnras/stz2355)
- Rosen, A. L. 2022, *ApJ*, 941, 202, doi: [10.3847/1538-4357/ac9f3d](https://doi.org/10.3847/1538-4357/ac9f3d)
- Schneider, F. R. N., Sana, H., Evans, C. J., et al. 2018, *Science*, 359, 69, doi: [10.1126/science.aan0106](https://doi.org/10.1126/science.aan0106)
- Schuller, F., Menten, K. M., Contreras, Y., et al. 2009, *A&A*, 504, 415, doi: [10.1051/0004-6361/200811568](https://doi.org/10.1051/0004-6361/200811568)
- Smith, R. J., Treß, R. G., Sormani, M. C., et al. 2020, *MNRAS*, 492, 1594
- Stutz, A. M. 2018, *MNRAS*, 473, 4890, doi: [10.1093/mnras/stx2629](https://doi.org/10.1093/mnras/stx2629)
- Traficante, A., Jones, B. M., Avison, A., et al. 2023, *MNRAS*, doi: [10.1093/mnras/stad272](https://doi.org/10.1093/mnras/stad272)
- Vázquez-Semadeni, E., Gómez, G. C., Jappsen, A. K., et al. 2007, *The Astrophysical Journal*, 657, 870
- Vázquez-Semadeni, E., Gómez, G. C., Jappsen, A. K., Ballesteros-Paredes, J., & Klessen, R. S. 2009, *ApJ*, 707, 1023, doi: [10.1088/0004-637X/707/2/1023](https://doi.org/10.1088/0004-637X/707/2/1023)
- Vázquez-Semadeni, E., Zamora-Avilés, M., Galván-Madrid, R., & Forbrich, J. 2018, *MNRAS*, 479, 3254, doi: [10.1093/mnras/sty1586](https://doi.org/10.1093/mnras/sty1586)
- Vázquez-Semadeni, E., Palau, A., Ballesteros-Paredes, J., Gómez, G. C., & Zamora-Avilés, M. 2019, arXiv preprint arXiv:1903.11247
- Walch, S., Girichidis, P., Naab, T., et al. 2015, *MNRAS*, 454, 238, doi: [10.1093/mnras/stv1975](https://doi.org/10.1093/mnras/stv1975)
- Wang, K., Zhang, Q., Testi, L., et al. 2014, *MNRAS*, 439, 3275, doi: [10.1093/mnras/stu127](https://doi.org/10.1093/mnras/stu127)
- Williams, T. G., Baes, M., De Looze, I., et al. 2019, *MNRAS*, 487, 2753, doi: [10.1093/mnras/stz1441](https://doi.org/10.1093/mnras/stz1441)
- Ysard, N., Juvela, M., Demyk, K., et al. 2012, *A&A*, 542, A21, doi: [10.1051/0004-6361/201118420](https://doi.org/10.1051/0004-6361/201118420)
- Zamora-Avilés, M., Vázquez-Semadeni, E., Körtgen, B., Banerjee, R., & Hartmann, L. 2018, *MNRAS*, 474, 4824, doi: [10.1093/mnras/stx3080](https://doi.org/10.1093/mnras/stx3080)
- Zamora-Avilés, M., Vázquez-Semadeni, E., González, R. F., et al. 2019, *MNRAS*, 487, 2200
- Zucconi, A., Walmsley, C., & Galli, D. 2001, *Astronomy & Astrophysics*, 376, 650